



University of L'Aquila

Department of Physical and Chemical Sciences

Sapienza University of Rome

Department of Information engineering, Electronics and Telecommunications

Department of Physics

Department of Civil, Environmental and Construction Engineering

Master of Science in Atmospheric Science and Technology
Master Thesis

Evan David Wellmeyer

Tropical Cyclone Triggering Mechanisms Synoptic and Numerical Analysis

Supervisor Prof. Rossella Ferretti

Co-supervisor Prof. Antonio Ricchi

Evan David Wellmeyer
(Student N.: 274892)

Academic Year 2022/2023

Abstract

This thesis investigates the conditions leading to the rapid intensification (RI) phase and maximum intensity of Hurricane Wilma during the 2005 North Atlantic hurricane season.

The study assesses the impact of climate-induced sea surface temperature anomalies (SSTA) on intensification using numerical model simulations that incorporate ocean mixed layer depth (OMLD). Hypothesizing that ocean heat content (OHC) and anomalously high sea surface temperatures (SSTs) in the Caribbean Sea trigger the observed RI phase, the objective is to quantify the contribution of SSTAs through numerical simulations.

The research begins with a preliminary analysis of seasonal tropical cyclone energetics, considering Accumulated Cyclone Energy (ACE) and the frequency of observed RI phases. Synoptic and oceanic conditions during genesis and intensification are examined using European Centre for Medium-Range Weather Forecasts (ECMWF) ERA5 Reanalysis and NOAA satellite-derived measurements. Numerical simulations with the Weather Research and Forecasting (WRF) model, initialized with SST fields consistent with observations (NORM run) and with SST fields excluding SSTA (MOD run), aim to isolate and quantify SSTAs' contribution.

The simulations successfully reproduce the RI phase and intensity trajectory, demon-

strating that SSTA significantly contributes to the analyzed aspects of Hurricane Wilma's intensity and track. It is found that the SSTA produces on average a 27% lower central sea level pressure (CSLP), a 30% difference in minimum CSLP, and a mean difference in maximum wind speed of about 6%. Furthermore, SSTA enhances the deepening rate during the RI phase by approximately 47% and increases the total surface heat flux by about 19%. It is also found that the SSTA produces a 10% increase in accumulated grid scale precipitation (RAINNC). The study concludes that SSTA has a substantial impact on both the intensity and track of the simulated tropical cyclone.

Despite certain discrepancies between simulated values and theoretical predictions, this study contributes valuable insights into the influence of SST on tropical cyclones. Recognizing limitations, including model resolution and simplifications in atmospheric adjustments, the study recommends using coupled models to identify mechanisms contributing to RI events. A broader analysis of multiple cases and an investigation into the joint contribution of surface fluxes and convective bursts are suggested to enhance the understanding of tropical cyclone intensification. The findings underscore the potential implications of climate-induced SSTAs on extreme rapid intensification events and highlight the need for further research to predict future changes in tropical cyclone frequency and intensity.

To Cosmo,

In the first weeks of your life I have assembled this work.

Contents

1	Introduction	11
2	Literature Review	15
2.1	Climatology of The Tropical Regions	15
2.2	Statistical Analysis	17
2.3	Energy, Air-Sea Interaction and Ocean Mixing	19
2.4	Case Study: Hurricane Wilma	23
3	Methodology	24
3.1	Model Configuration	26
3.2	Post-processing	29
4	Preliminary Analysis	30
4.1	Statistical Analysis	30
4.2	Case Study Analysis	33
4.2.1	Genesis and Intensification - Synoptic Overview	35
4.2.2	Ocean Analysis	40

5 Simulation Results	42
5.1 Initialization Fields	43
5.2 Accumulated Cyclone Energy Index	43
5.3 TC Displacement	44
5.4 Pressure, Wind and Deepening Rate	46
5.5 Heat Flux and Precipitation	47
5.6 Energy Extracted from the Surface	50
5.7 Ocean Mixed Layer Depth	51
5.8 Impact of SSTA	52
6 Conclusion	55
A Eyewall Evolution	65

List of Figures

2.1 Schematic showing relationship between MLD, D26 and OHC. The red shading shows the true OHC as the integral of the black temperature profile. The blue dashed line shows the approximate thermal profile to D26. Figure adapted from (Shay et al., 2022)	22
3.1 Domain configuration used for WRF Model, with a coarse resolution of 9 km and a nested domain resolution of 3 km.	27
4.1 Number of TC occurrences every year (top) and calculated accumulated cyclone energy per year (bottom) during the period 1961-2022 according to the HURDAT2 database.	31
4.2 Distribution of Tropical Disturbances with and without Rapid Intensification in the period 1961-2022, calculated from HURDAT2.	32
4.3 The anomalies for (a) Sea Surface Temperature (1880-2022) from 1901-2000 average in °C and (b) 0-700m Ocean Heat Content (1955-2023) from 1955-2006 average. Downloaded from NOAA Climate.gov.	33

4.4 Reported observations for Hurricane Wilma showing a) the partial path of the storm with color according to CSLP at each observation and location of maximum DR, and b) the timeseries of CSLP (left), maximum sustained wind speed (middle), and calculated DR (right) derived from the HURDAT2 dataset.	34
4.5 Atmospheric parameters conducive to TC formation as reported in Section 2.1, 48 hours before identification of the localized pressure system to later become Hurricane Wilma. Reported values are a) the mean sea level pressure (contours) with 850 hPa temperature (color), b) SST, c) wind shear between the 200 hPa and 500 hPa levels, d) averaged 975 hPa to 750 hPa relative vorticity, e) mean lapse rate between the 975 hPa and 200 hPa levels, and f) averaged 925 hPa to 200 hPa relative humidity, from ERA5 Reanalysis.	36
4.6 Vertically integrated water vapor flux on 12 October 18UTC in both magnitude and vector form, from ERA5 Reanalysis.	37
4.7 Mean Sea Level Pressure (contours) with 850 hPa temperature (color) at a) 15 October 00UTC, b) 17 October 00UTC, c) 18 October 18UTC, d) 19 October 00UTC, e) 19 October 06UTC and f) 19 October 12UTC from ERA5 Reanalysis.	39
4.8 Sea Surface Temperature Anomaly in °C for (a) 15 October 18UTC and (b) 24 October 00UTC from 1985-2005 reference mean, calculated from ERA5 reanalysis. Hurricane Wilma track and position at respective times sourced from hurdat dataset.	40
4.9 The satellite derived (a) Mixed Layer Depth, b) 26°C Isotherm Depth and (c) Ocean Heat Content on 18 October 2005 from NOAA (Donahue, 2015). Downloaded from Miami Rosenstiel School.	41

5.1	Sea surface temperature initialization fields for the two simulations, with the left figure representing the observed SST field and the right figure as the SST field after subtracting the 1985-2005 anomaly.	43
5.2	Calculations for ACE index for the two simulations and observational values for HURDAT2 during the period 18-22 October 00UTC.	44
5.3	Trajectory of minimum pressure (solid lines) with minimum pressure values at each model output time (colored points) for the two simulations. The black solid line indicates the NORM run, and the red solid line indicates the MOD run. The observational trajectory from NOAA during the same time period is also shown as a dotted black line.	45
5.4	Timeseries' of minimum CSLP (left), maximum wind speed (middle) and DR (right) for the two WRF simulations. The solid black line indicates values for the NORM run, and the dashed line indicates values for the MOD run.	46
5.5	Timeseries' of maximum Total Surface Heat Flux (left) and maximum Accumulated Total Grid Scale Precipitation (right) for the two WRF simulations. The solid black line indicates values for the NORM run, and the dashed line indicates values for the MOD run.	48
5.6	WRF simulations results for a) total heat flux at the time of maximum TC intensity (20 October 15 UTC) and b) the accumulate total grid scale precipitation at 22 October 00UTC.	49
5.7	Calculated heat transferred from the surface to the atmosphere in a 330 km radius of the minimum CSLP location for the two simulations.	50
5.8	WRF simulation results for Ocean Mixed Layer Depth (OMLD) at the end of the simulation period (22 October 00UTC).	51

5.9 The contribution of the SSTA to the intensity and overall energy extraction represented as a percentage difference between the NORM and MOD simulation results.	53
A.1 WRF model outputs showing the evolution of the eyewall at 3 hour intervals with respect to maximum wind speed for a) the simulation using observational SST initialization fields and b) the simulation where the 1985-2005 SSTA has been subtracted.	66
A.2 WRF model outputs showing the evolution of the eyewall at 3 hour intervals with respect to total heat flux for a) the simulation using observational SST initialization fields and b) the simulation where the 1985-2005 SSTA has been subtracted.	67

1

Introduction

Among the most spectacular and enigmatic features of the tropical atmosphere are the violently rotating circulations that occasionally form over the warmest parts of the tropical oceans.

Kerry Emanuel

The analysis of mechanisms triggering the rapid intensification (RI) of tropical cyclones (TCs) stands as a paramount research endeavor, given the significant impact these storms can have on coastal regions. TCs, among the largest and most destructive natural phenom-

ena, necessitate a thorough understanding of their intensity dynamics, particularly during landfall, to enhance preparation and mitigation efforts.

Despite the extensive study of TCs, the processes underlying RI phases, characterized by substantial intensity changes over short durations, remain a critical area requiring deeper exploration. The year 2005 marked a historic hurricane season, notable for both the sheer number of storms and the unprecedented power they exhibited. In this context, Hurricane Wilma set a North Atlantic basin record for the lowest pressure after undergoing a remarkable RI phase.

A number of studies have performed numerical analysis on Hurricane Wilma (Vincente, 2010; Chen et al., 2011; Chen and Zhang, 2013; Miller et al., 2015; Qin et al., 2018). The former attempts (Vincente, 2010) used both Hurricane WRF (H-WRF) and Advanced Research WRF (ARW) producing minimum central pressures of 999 mb and 978 mb, respectively, far from the observed RI and minimum central sea level pressure (CSLP) in Hurricane Wilma. A later study (Chen et al., 2011) was able to reproduce the observed RI reasonably well at 4 hPa h^{-1} over a 18 hour RI period and peak intensity of 889 hPa and 72 m s^{-1} using ARW with a quadruply nested grid. In addition to a relatively accurate representation of the intensification period, the simulation was also able to produce the observed Eyewall Replacement Cycle (ERC), where a secondary eyewall forms resulting in a dissipation of the primary eyewall and associated decrease in intensity. Subsequent studies using the same model setup and results focused on the development of the upper-level warm core and their relationship to convective bursts, and the relative dependence of these and RI on sea surface temperatures (SSTs) (Chen and Zhang, 2013); the impact of upper-level latent heat of deposition on structure and intensity changes (Miller et al., 2015); and characteristics of the inner-core vortex structures and the relationship between RI and eyewall contraction (Qin et al., 2018).

While the general mechanisms sustaining TCs are well-established, there exists a significant gap in understanding how ocean heat content (OHC), ocean mixed layer depth (OMLD), and anomalously higher SSTs, attributed to climate change, contribute to RI. Notably, the specific role of these oceanic factors in the case of Hurricane Wilma has not been comprehensively studied.

This thesis aims to address this gap by first providing an overview of the synoptic conditions in which Hurricane Wilma was embedded. Subsequently, a series of numerical simulations will be conducted to discern the distinct roles played by OHC, OMLD, and SST anomalies (SSTAs) in the RI of TCs. By investigating these factors, this research seeks to contribute to a better understanding of how a changing climate may influence the intensification dynamics of TCs.

The thesis is structured as follows: Chapter 2 contains an introduction and review of literature on a range of subjects, with Section 2.1 giving an introduction to the tropic region and TCs, Section 2.2 considers how statistical classifications of TCs can be performed considering Accumulated Cyclone Energy (ACE) and Deepening Rate (DR), Section 2.3 introduces the energy cycle of TCs, their sources of energy and how these can be modulated by ocean conditions, and Section 2.4 introduces the case study. Chapter 3 contains the methodology used in this study, introducing the datasets used and the periods referenced, with Section 3.1 introducing the philosophy of the numerical approach used and the subsequent model setup, and Section 3.2 covering the algorithms constructed for the post-processing of the numerical simulations. Chapter 4 contains an analysis of the synoptic and ocean conditions, with Section 4.1 applying the statistical approach introduced in Section 2.2, as well as climatological considerations for ocean variables. Section 4.2 focuses on synoptic and ocean aspects of the case study, beginning with an analysis of observational records. Section 4.2.1 gives an overview of synoptic conditions during the genesis and intensification of

the storm. Section 4.2.2 considers the state of the sea before and after the storms passing referencing both satellite derived values and reanalysis. Finally, Chapter 5 considers the numerical simulation results with reference to all aspects discussed prior, identifying the role of SSTA.

The numerical simulations successfully reproduce the RI and maximum intensity of Hurricane Wilma. Results indicate that SSTA significantly contributes to various aspects of the TC's intensity and displacement. The study reports a substantial impact of SSTA on minimum central sea level pressure (CSLP), maximum wind speed, DR, and surface heat flux. Moreover, the findings reveal the influence of SSTA on precipitation and energy transfer, emphasizing the multifaceted role of SST in TC intensification.

While acknowledging discrepancies between simulated values and theoretical predictions, the study underscores the remarkable influence of relatively small differences in SST on simulated TC characteristics. It provides valuable insights into the manifestation of extreme RI phases, as observed in recent events like Hurricane Otis in October 2023. Additionally, the research highlights the massive energy extraction from oceans during intense TCs, considering the potential implications in the context of climate-induced changes.

Acknowledging the limitations, including model resolution and singular focus on a specific RI case, the study proposes future enhancements. Recommendations include considering multiple cases, employing coupled models for a deeper understanding of contributing mechanisms, and exploring the joint impact of surface fluxes and convective bursts. These proposed advancements aim to refine our understanding of TC intensification, contributing to improved forecasting models and a more comprehensive grasp of RI phenomena.

2

Literature Review

2.1 Climatology of The Tropical Regions

The tropics encompass a region of earth near the equator, stretching between the Tropic of Cancer and the Tropic of Capricorn at approximately 23.5 degrees north and south of the equator. These are defined by the furthest latitude north reaching normal to the sun during the June Solstice and the furthest latitude south reaching normal to the sun during the December Solstice. The tropics experience a warm, humid climate characterized by consistent high temperatures and relatively minimal diurnal and seasonal fluctuations. This climate

results from the abundant solar energy received year-round, which significantly influences both the atmospheric and oceanic conditions in the region.

Yearly variability in the tropics is intrinsically tied to the behavior of the Intertropical Convergence Zone (ITCZ). The ITCZ is a dynamic belt of convergence where trade winds from both hemispheres meet, leading to the upward movement of warm, moist air. The ITCZ serves as a meteorological equator of sorts, influencing the region's climate. The ITCZ shifts north and south as the Earth's axial tilt changes throughout the year, resulting in a distinct wet and dry season pattern in many tropical areas. As the ITCZ shifts, it causes variations in atmospheric conditions, cloud cover, and precipitation patterns, impacting both the meteorology and oceanography of the region. The climatic oscillations driven by the ITCZ significantly affect ocean temperatures, currents, and marine ecosystems, making the tropics a region of great oceanographic complexity.

A meteorological phenomenon that is particularly pronounced in the tropical region and influenced by the ITCZ are Tropical Cyclones (TCs). TCs can be defined as non-frontal synoptic scale low-pressure systems over tropical waters with organized deep convection and definite cyclonic surface wind circulation (Holland and Lander, 1993). These cyclones depend on the warm ocean temperatures and the latent heat of condensation released during the process of convection, creating low-pressure systems that can rapidly intensify under the right conditions. The ocean's thermal structure plays a critical role in the development and intensification of TCs. Understanding the meteorological, climatological, and oceanographic intricacies of the tropics and their direct impact on TCs is essential for predicting and mitigating the devastating effects of TCs in these regions.

There are several "basins" distributed north and south of the equator around the globe, representing locations where specific conditions can be met at certain times of the year for TC genesis (cyclogenesis). Some of the most basic conditions necessary for cyclogenesis

to occur have been established. These include some independent near surface disturbance (Riehl, 1948), warm ocean temperatures of at least 26°C (Palmen, 1948), low vertical wind shear and positive low-level vorticity (Gray, 1968; Tory et al., 2013), at least 5° of latitude for sufficient values of the Coriolis parameter, high mid-troposphere lapse rate and sufficient mid-troposphere humidity (Gray, 1979; Takemi and Yamasaki, 2020).

2.2 Statistical Analysis

Approximately 80 TCs develop every year among the seven basins, a number that remains steady despite sometimes significant fluctuations in specific basins year over year (Ramsay, 2017). The TC activity in a particular basin can be assessed each year from an energetic standpoint through the Accumulated Cyclone Energy (ACE). The ACE index was originally introduced as the Hurricane Destruction Potential to provide an estimate of potential damage from a storms wind and storm surge (Gray, 1988). This formula was later revised into the ACE index to give a comprehensive view of overall TC activity in a season (Bell et al., 2000). ACE calculations are based on a formula that considers the maximum sustained wind speed of each TC at six-hour intervals over its lifetime, considering only intervals where the maximum wind speed exceeds 35 knots. The square of these maximum wind speed is summed for each time interval, accounting for both the duration and intensity of the storm. The ACE index is represented as follows:

$$\text{ACE} = 10^{-4} \sum v_{max,v>35}^2 \quad (2.1)$$

By adding these values for all cyclones within the designated region and time frame, the ACE index can quantify the total kinetic energy produced by either a single or multiple storms.

TCs can further be classified statistically through a Rapid Intensification (RI) index. The RI classification is useful in selecting case studies of interest for numerical analysis, as a RI phase could potentially be found in an otherwise insignificant storm. RI cases are especially important features to study in TCs since large changes in intensity before landfall can have serious consequences. The RI characterization was first introduced by Tor Bergeron in regards to rapidly deepening extratropical lows with a deepening rate (DR) of at least 1 mb h⁻¹ over a 24 hour period (Bergeron, 1954), referred to as an explosive cyclogenesis (EC). The definition for DR of ECs was later extended by the authors (Sanders and Gyakum, 1980) by multiplying the change in pressure over a time period by a latitude term in order to obtain a geostrophically equivalent rate for an arbitrary latitude:

$$1 \text{ Bergeron} = \frac{24 \text{hPa}}{24 \text{h}} \left(\frac{\sin \phi}{\sin 60^\circ} \right) \quad (2.2)$$

with ϕ as the latitude of the cyclone. The latitude term takes into account the same radial pressure gradient yielding a higher (lower) velocity at lower (higher) latitudes. The definition provided by the authors (Sanders and Gyakum, 1980) was further modified in subsequent studies shifting the reference latitude to the average of the phenomenon of interest (Roebber, 1984; Gyakum et al., 1989) and adjusting the deepening period to 12 hours in order to take advantage of higher frequency data samples (Yoshida and Asuma, 2004; Zhang et al., 2017; Carniel et al., 2023):

$$\text{DR} = \left(\frac{P_{t-6h} - P_{t+6h}}{12} \right) \left[\frac{\sin 45^\circ}{\sin \left(\frac{\phi_{t-6h} + \phi_{t+6h}}{2} \right)} \right] \quad (2.3)$$

with P and ϕ as the pressure and latitude of the cyclone at 6 hours before and after, respectively. This method centers the calculation index between the indices of the variables in use. The definition of RI was later reevaluated to be applied to TCs and defined as approx-

imately the 95 percentile of all 24-hour over-water intensity changes of Atlantic basin TCs, which equated to a maximum sustained wind speed increase of 15.4 ms^{-1} (30 knots) for a 24 hour period (Kaplan and DeMaria, 2003), which translates to a DR of approximately 1.5 hPa h^{-1} over a 24 hour period through geostrophic equivalence (Chen et al., 2011).

2.3 Energy, Air-Sea Interaction and Ocean Mixing

It has been demonstrated that the energy cycle of a mature TC is similar to an ideal Carnot engine, undergoing a cycle of isothermal expansion (with the addition of enthalpy), adiabatic expansion, isothermal compression, and adiabatic compression (Emanuel, 1986, 2003). The energy driving this cycle comes mainly in the form of heat transfer from the ocean through enthalpy fluxes (Riehl, 1950; Kleinschmidt, 1951; Malkus and Riehl, 1960; Riehl, 1963). Air spiraling into the TC undergoes a drop in pressure and its entropy increases due to enthalpy transfer (latent heat of vaporization) from the sea surface as well as dissipation of kinetic energy (Bister and Emanuel, 1998). The air-sea transfer of heat input and dissipation of kinetic energy are quantified by flux of enthalpy (F_k) from the sea and flux of momentum (F_m) into the sea using the bulk formulae:

$$\begin{aligned} F_k &= C_k \rho |V| (k_0^* - k) \\ F_m &= -C_D \rho |V| V \end{aligned} \tag{2.4}$$

with V as the near-surface wind speed, ρ as the air density, C_k and C_D are the transfer coefficients (dimensionless) of enthalpy and momentum, respectively, k is the specific enthalpy of air near the surface, and k_0^* is saturation enthalpy of the sea surface (Bister and Emanuel, 1998; Emanuel, 2003). Based on the dependence of a TC on enthalpy fluxes from the sea surface, which subsequently depend on SST, it has also been shown (Bister and Emanuel, 1998) that an approximate expression for maximum wind speed can be obtained dependent

on the SST:

$$|V_{\max}|^2 \approx \frac{C_k}{C_D} \frac{T_s - T_0}{T_0} (k_0^* - k) \quad (2.5)$$

with T_s as the SST and T_0 as temperature at the tropopause. An expression for the characteristic timescale, τ , over which the vortex evolves has also been established (Emanuel, 1989):

$$\tau \approx \frac{H}{C_D V_{\max}} \quad (2.6)$$

with H as the atmospheric scale height and V_{\max} given by Equation 2.5, so that both maximum intensity of a TC and the possibility of it undergoing a RI phase are dependent on SST, among other requirements of a conducive environment.

Several studies have investigated the sensitivity of TCs to SSTs, examining both intensification and weakening processes. While the enthalpy fluxes from the sea surface play a crucial role in providing energy for the growth and maintenance of TCs, this induces a reduction of SST beneath the TC and the formation of a cold wake (Leipper, 1967). TCs have been found to exhibit a high sensitivity to these reductions in SST below the eye, resulting in a negative feedback mechanism for TC intensity (Schade and Emanuel, 1999; Schade, 2000). Studies investigating the SST cooling following TCs find an average decrease in energy of 12 kJ cm^{-2} in the top 100m of the sea (Knaff et al., 2013).

In the context of intensification, an early study deduced a sensitivity of the maximum potential intensity (MPI) in a TC to SST of $10 \text{ hPa } ^\circ\text{C}^{-1}$ (Emanuel, 1988). However, subsequent research contrasted this with a proposed sensitivity of MPI of $33 \text{ hPa } ^\circ\text{C}^{-1}$ (Holland, 1997). This apparent discrepancy was later clarified (Schade, 2000), interpreting the earlier study as more relevant to the sensitivity of MPI under equilibrium conditions, where the tropical atmosphere had adjusted to the SST, while the latter study examined deviations in SST that the atmosphere had not adapted to.

Recent studies employing numerical models have advanced our understanding of SST's impact on both the intensity and track of TCs (Mandal et al., 2007), as well as its role in the onset and magnitude of RI events (Chen et al., 2018). The previous author found that a 1°C decrease in SST can delay the onset of an RI phase by ~13 hours. Furthermore, the mechanisms by which SST contributes to RI phases have been explored in recent literature, indicating that higher SSTs produce greater heat fluxes, and that these elevated heat fluxes induce a stronger overturning circulation in the low to middle troposphere, resulting in a more rapid spin-up of TCs (Črnivec et al., 2016). In addition to these considerations, recent research has highlighted that multiple factors can induce RI episodes in TCs without solely relying on anomalously high surface heat fluxes (Judt et al., 2023). This emerging perspective adds a nuanced layer to our understanding of the complex interactions influencing TC intensification dynamics.

The ocean mixed layer (OML) is a quasi-homogeneous region in the upper ocean characterized by little variation in temperature or density with depth (Kara et al., 2000). If temperatures surpass 26°C through a sufficient depth, the OML acts as a heat reservoir for TC growth and maintenance (Mao et al., 2000). The OML can diminish the negative feedback by replenishing the energy to the sea surface that has been extracted, allowing further heat exchange to drive the TC (Lin et al., 2005). It has also been shown that when ocean mixed layer depth (OMLD) increases toward the west, the entrainment of cooler water into the mixed layer from below is moderated and the TC can develop to greater intensity (Mao et al., 2000). The authors also showed that when a TC moves into an increasingly deep mixed layer, it develops to greater intensity than for a mixed layer of constant depth.

The perspective of the OML shows us not only the SST is important, but also the Ocean Heat Content (OHC). The OHC, which has been referred to previously as Hurricane Heat Potential (Leipper and Volgenau, 1972) and Tropical Cyclone Heat Potential (TCHP) (Wada

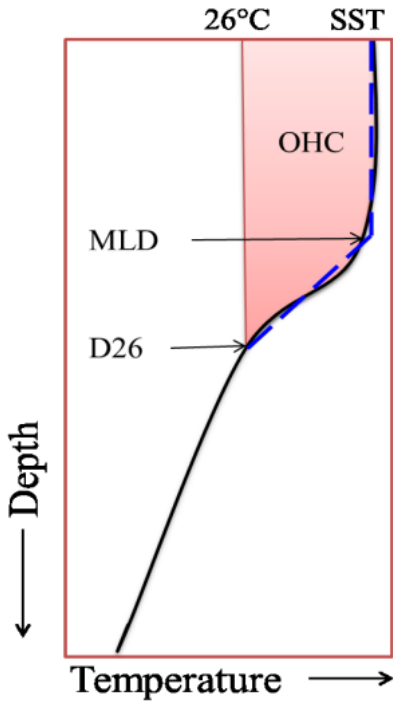


Figure 2.1: Schematic showing relationship between MLD, D26 and OHC. The red shading shows the true OHC as the integral of the black temperature profile. The blue dashed line shows the approximate thermal profile to D26. Figure adapted from (Shay et al., 2022).

and Chan, 2008), is defined as:

$$\text{OHC} = \sum_{h=0}^{Z_{26}} \rho_h C_p (T_h - 26) \Delta Z_h \quad (2.7)$$

with ρ_h as the density of the water at each layer, C_p is the specific heat capacity, T_h is the water temperature in °C at each layer, ΔZ_h is the thickness of each layer and Z_{26} is the depth of the 26°C isotherm (D26). The term in parentheses ($T_h - 26$) makes the OHC the amount of excess energy in the layer (per area of the surface) that could theoretically be removed while the minimum SST threshold of 26°C for TC formation and maintenance is sustained.

A schematic for the relationship between the terms OMLD (aka MLD), OHC and D26 is presented in Figure 2.1. As previously stated, the dissipation of kinetic energy in a TC also happens through flux of momentum into the sea, resulting in increased upper ocean mixing. While the previous study indicated this induces cold upwelling and surface cooling, a high

OHC from D26 sufficiently below the OML would theoretically result in the upwelling of more TC conducive temperature water into the OML from below.

2.4 Case Study: Hurricane Wilma

The tropical depression (TD) that would later become Hurricane Wilma formed October 15, 2005 south of Jamaica following an unusually large, monsoon-like lower-tropospheric circulation over the Caribbean Sea, which was enhanced by flow to the south and southwest by an upper-level cyclone which lead to a more concentrated area of disturbed weather and low surface pressure near Jamaica by October 14 (Pasch et al., 2006). The well defined surface circulation granted TD classification by 1800 UTC 15 October. The storm moved slowly southwest over the next two days, while low-level southwesterly moisture supplied from the ITCZ allowed continuous organization of convective clouds (Chen et al., 2011). During this period the TD slowly strengthened into a tropical storm (TS) by 0600 UTC 17 October (Pasch et al., 2006). The storm then turned northwest on October 18, strengthening into a hurricane as a large moisture supply triggered and intense convective burst on the southern side of the cyclonic circulation (Pasch et al., 2006; Chen et al., 2011). A 12 hour RI episode began approximately 1800 UTC 18 October when Hurricane Wilma crossed an area of high Ocean Heat Content (OHC), resulting in a central pressure decrease of 29 hPa in the first 6 hours and a subsequent 54 hPa decrease in the following 6 hours (Chen et al., 2011). During the RI process, Air Force reconnaissance observations indicated the eye of Wilma contracted to approximately 4 km, the smallest eye known to the staff of the National Hurricane Center (NHC) (Pasch et al., 2006). By 0600 UTC 19 October, Hurricane Wilma's winds reached 150 knots, with peak sustained winds of 160 knots at approximately 1200 UTC 19 October, and a central pressure of 882 hPa—the lowest central pressure on record for the Atlantic basin (Pasch et al., 2006; Chen et al., 2011).

3

Methodology

This investigation of the oceans impact on TCs will be provided from three different points of view. The first step is a statistical analysis of tropical cyclones in the North Atlantic basin considering both ACE and DR and an assessment of the global trend in SST and OHC. The second part is an overview of Hurricane Wilma on a synoptic scale using both the Nation Oceanographic and Atmospheric Administration (NOAA) and National Hurricane Centers (NHC) Atlantic hurricane database "HURDAT2" dataset (Landsea and Franklin, 2013) and the European Centre for Medium-Range Weather Forecasts (ECMWF) ERA5 Re-

analysis (Hersbach et al., 2023b,a). The third part will consider two numerical simulations of Hurricane Wilma. The HURDAT2 dataset currently spans from 1851 to 2022 and includes a range of parameters at 6 hourly intervals for each individual tropical cyclone on record. Due to a potentially under representation of TC statistical records before satellite observations began with the launch of TIROS-1 in 1960, analysis regarding the number of storms in the selected basin will span from 1961, when satellite observations began to account for virtually all tropical cyclone instances. Moreover, due to lack of sufficient data included in the dataset for storms before 1992, statistical analysis regarding individual storm intensity will span from then to present. Analysis of global anomalies for SST and OHC reference figures downloaded from the NOAAs Global Climate Dashboard.

Synoptic, Oceanic and Numerical analysis will be provided for a rapid intensification case study. The synoptic analysis will be based on ECMWF ERA5 Reanalysis, the fifth generation global atmospheric reanalysis dataset that combines model data with observations from across the world into a globally complete and consistent dataset through data assimilation. The resulting dataset used is available at temporal resolution of 1 hour and a horizontal spatial resolution of 30 km, with atmospheric variables resolved on 137 levels and output at 37 pressure levels (plus surface) from the surface to an altitude of approximately 80 km. The ERA5 dataset currently spans from 1940 to present. Satellite derived measurements provided by NOAA are also used to assess the ocean conditions around the time of the RI phase.

The numerical analysis will be performed using the Weather Research and Forecasting (WRF) model/Advanced Research WRF (ARW). The WRF model is a fully compressible and nonhydrostatic numerical model that can utilize both terrain following or hybrid vertical hydrostatic pressure coordinates on an Arakawa C staggered grid. The WRF model is used because it is a state of the art atmospheric simulation system, suitable for applications of

a broad range of scales and resolutions. WRF has been produced and upgraded through collaborative efforts since the late 1990s by the National Center for Atmospheric Research (NCAR), NOAA, the Air Force Weather Agency (AFWA), the Naval Research Laboratory (NRL), University of Oklahoma, and the Federal Aviation Administration (FAA). The WRF model has received many upgrades over the years, becoming one of the most widely used numerical weather prediction (NWP) systems for both atmospheric research and operational forecasting.

3.1 Model Configuration

Two separate WRF simulations are analyzed. Both simulations use a nested domain configuration, with the coarse domain at a resolution of 9 km, and the nested domain at 3 km. Both domains used 75 vertical eta levels, with the top level at 50 hPa. The boundaries for the coarse and nested domains are shown in Figure 3.1. The number of grid points used for the domains is 445 by 357 for the coarse domain and 976 by 778 for the nested domain.

The WRF `namelist.input` configuration settings of interest are present in Table 3.1. The WRF setting was as follows. The ocean mixed layer physics (`oml_hml0`) in both simulations is set to a simple ocean mixed layer option, a one-dimensional approach where each column is independently coupled to the local atmospheric column, and comprises a time-varying layer with variable-depth over a fixed reservoir of cooler water (Pollard et al., 1973). This option considers the depth, vector horizontal current, and mean temperature (taken to be the SST) of the OML. By incorporating the OML into the model, energy (TCHP) held in the OML serves to reinforce the heat flux from the sea surface, allowing more energy available for extraction before dramatic changes in the SST occur; however, this option also considers that as hurricane winds drive the current, it induces mixing at the base of the mixed layer, both deepening and cooling it. In order to address this, the model in-

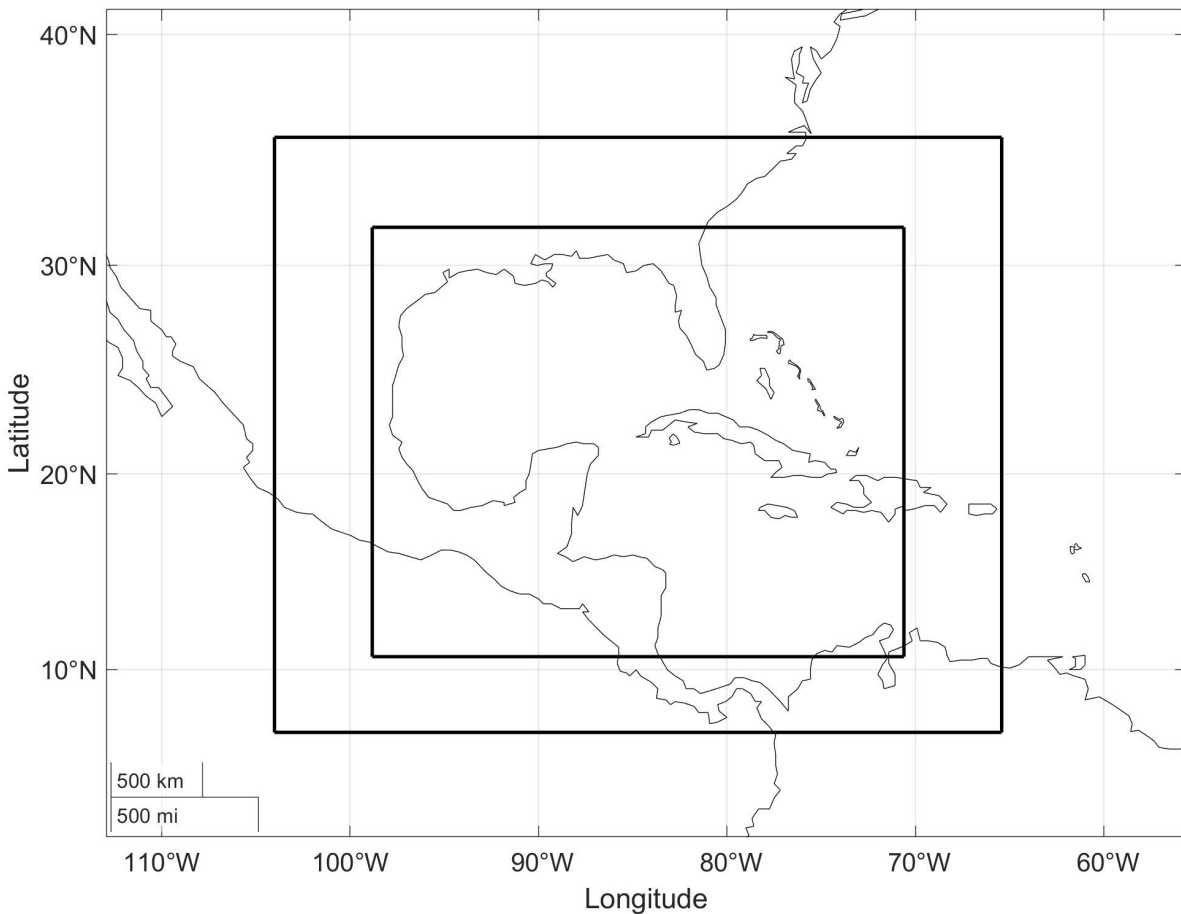


Figure 3.1: Domain configuration used for WRF Model, with a coarse resolution of 9 km and a nested domain resolution of 3 km.

corporates a heat budget for the OML. Coriolis effects on the current are also included, so that the location of maximum cooling is on the right side of the hurricane track (Skamarock et al., 2008). Both simulations are initialized with OMID at 75 meters in approximate agreement with observed values, as reported in Chapter 4. The `time_step` option has been reduced to twice the resolution from the typical `6*dx` due to the intensity of the TC. The microphysics option, `mp_physics`, determines the atmospheric heat and moisture tendencies and includes explicitly resolved water vapor, cloud and precipitation processes. The selected microphysics scheme is the WRF Double-moment 6-class (WDM6) scheme that includes double-moment rain, and cloud and CCN for warm processes in addition to ice, snow and graupel processes (Lim and Hong, 2010). The planetary boundary layer (PBL) option (`bl_pbl_physics`) is responsible for vertical sub-grid-scale fluxes due to eddy transports

in the whole atmospheric column. The selected PBL option is the Mellor-Yamada-Janjić (MYJ) scheme, a one-dimensional prognostic turbulent kinetic energy scheme with local vertical mixing (Mesinger, 1993; Janjić, 1994). The cumulus parameterization schemes are responsible for the sub-grid-scale effects of convective and/or shallow clouds. They represent vertical fluxes due to unresolved updrafts and downdrafts and compensating motion outside of clouds. They also provide vertical heating and moistening profiles. The selected scheme is the Multi-scale Kain-Fritsch scheme that utilizes scale-dependent dynamic adjustment timescale, and LCC-based entrainment (Zheng et al., 2016; Glotfelty et al., 2019).

Setting	Value	Description
time_step	5	Temporal step for integration in seconds
e_vert	75	Number of vertical eta levels
p_top_requested	50	Top of model (hPa)
dx	9000,3000	Grid resolution (m)
dy	9000,3000	Grid resolution (m)
e_we	445,976	Number of grid points (west-east)
e_sn	357,778	Number of grid points (south-north)
mp_physics	16	WRF Double-moment 6-class
bl_pbl_physics	2	Mellor-Yamada-Janjić
cu_physics	11	Multi-scale Kain-Fritsch:
sf_ocean_physics	1	Simple ocean mixed layer
oml_hml0	75	Ocean Mixed Layer Depth

Table 3.1: WRF namelist.input configuration for parameters of interest. Cells with two values represent the settings for the coarse domain and the nested domain, respectively.

The first set of simulations cover a period of 192 hours, beginning from 14 October 00UTC and ending at 22 October 00UTC. This period covers the observed genesis, RI phase, and maximum intensity of Hurricane Wilma. For reasons explained later, a second set of simulations were performed, initializing on 18 October 00UTC and concluding 22 October 00UTC. The WRF model has been forced with the Global Forecast System (GFS) Final (FNL) 1 degree resolution (~ 110 km) global model. The global model provides 6 hourly outputs which have been used to update the boundary conditions on the WRF model coarse domain. The first simulation has been initialized with observed values for SST. The second simulation

uses observed SST values subtracting the SSTA from the period 1985-2005, which allows the analysis of RI in a TC in the context of a changing climate.

3.2 Post-processing

Post-processing of data is performed using the MATLAB scripting software. A tracking algorithm has been developed by which values can be extracted. In its simplest form, the tracking algorithm works by identifying the lowest mean sea level pressure (MSLP) in the domain and recording the location iteratively. A “mask” is applied over the area of the targeted low pressure system so that the algorithm looks for the movement of the low only inside that area during the next iteration. This simple method proves sufficient for the case of Hurricane Wilma according to preliminary tests with ERA5 data, as well as in most cases where a specific TC is already known to exist. The algorithm can be scaled, however, to identify either areas of potential cyclogenesis or multiple TCs within a domain. Identification of potential cyclogenesis can be done by setting minimum threshold “masks” over the entire domain, i.e. eliminating areas with SSTs lower than 26°C or high vertical wind shear, then the algorithm can identify areas where conditions are good for cyclogenesis, i.e. low MSLP and positive low-level vorticity. Once the location of TC is identified, variables may then be extracted at or within a radius with respect to the center. Timeseries’ of variables extracted from the WRF model simulations are those within a 60 km radius (square), equivalent to 40x40 grid points for the nested domain resolution, and centered on the minimum pressure position.

4

Preliminary Analysis

4.1 Statistical Analysis

For the Atlantic basin, an average of approximately 16 TCs developed each year during the period 1961-2022 according to the HURDAT2 database. During the same period, an average of 6.4 TCs reach hurricane strength, and 2.6 become major hurricanes (Category 3+). The distribution of TCs per year during the period 1961-2022, with the accompanying yearly calculations of ACE, are presented in Figure 4.1. From the period analyzed, the 2005 hurricane season is one of the most active hurricane seasons for number of storms and the

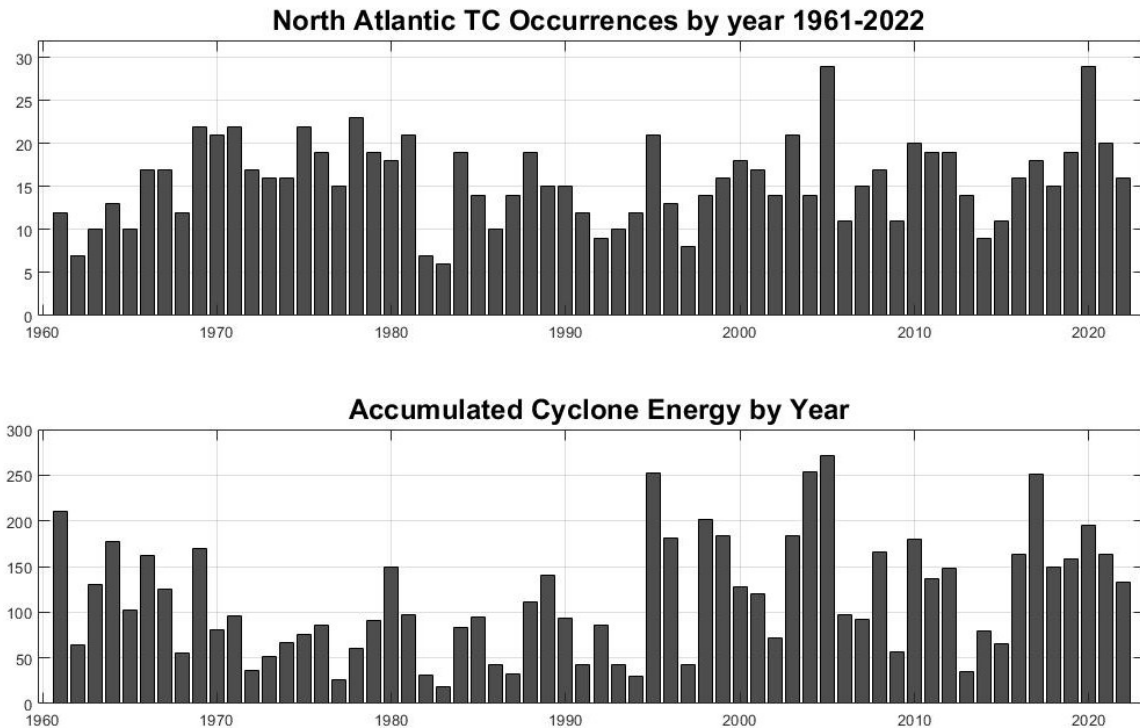


Figure 4.1: Number of TC occurrences every year (top) and calculated accumulated cyclone energy per year (bottom) during the period 1961-2022 according to the HURDAT2 database.

most active in the period according to ACE index. In this period there is also no clear signal for change in both number of storms or ACE per year.

The RI index has also been considered in a new way by combining the definitions from previous authors into an explicit definition for an arbitrary temporal DR, τ , of a TC in the Atlantic basin:

$$\text{DR} = \frac{2(P_{t-\frac{\tau}{2}} - P_{t+\frac{\tau}{2}})}{3\tau} \quad (4.1)$$

where the latitude term has been dismissed. Using this definition, if we set $\tau = 24$ hours, an average of 1 TC per year, equivalent to 6%, is calculated as undergoing a RI phase ($\text{DR} \geq 1$ Bergeron) during the 1961-2022 period in agreement with the previous authors intentions. The relative distribution of the storms strengths reported above is shown in Figure 4.2, with 61% of disturbances not reaching hurricane strength, and 23% and 10% of disturbances reaching non-major hurricane strength (Category 1-2) and major hurricane strength

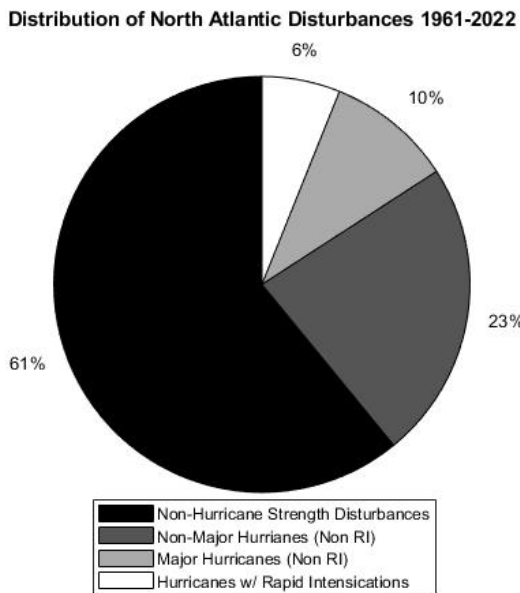


Figure 4.2: Distribution of Tropical Disturbances with and without Rapid Intensification in the period 1961-2022, calculated from HURDAT2.

(Category 3+) without undergoing RI phases, respectively.

The anomalies for SST during the period 1880-2022 and 0-700m OHC from 1955-2023 are presented in Figure 4.3. The SST anomaly (SSTA) here is calculated as the difference from the average during the period 1901-2000 in °C, and the OHC anomaly (OHCA) is calculated as the difference from the average during the period 1955-2006 in 10 ZJ (10^{22} J). It is important to note that the OHC here has been reported as total heat energy content in the 0-700m layer. While this definition is different than previously reported and how it will be referred to later on, for the purposes of this report the significance is the same. Both SSTA and OHCA show upward trends at a potentially exponential rate. With a global average increase of OHC on the order of 10^{22} J per year in the upper layer of the ocean, a TC, under the appropriate atmospheric conditions, has at its disposal more energy for intensification and maintenance when considered with SST feedback dampening by ocean mixing. We can also speculate that the entrainment of cooler water into the mixed layer from below is diminished as 26°C isotherm depths will increase with increasing OHC.

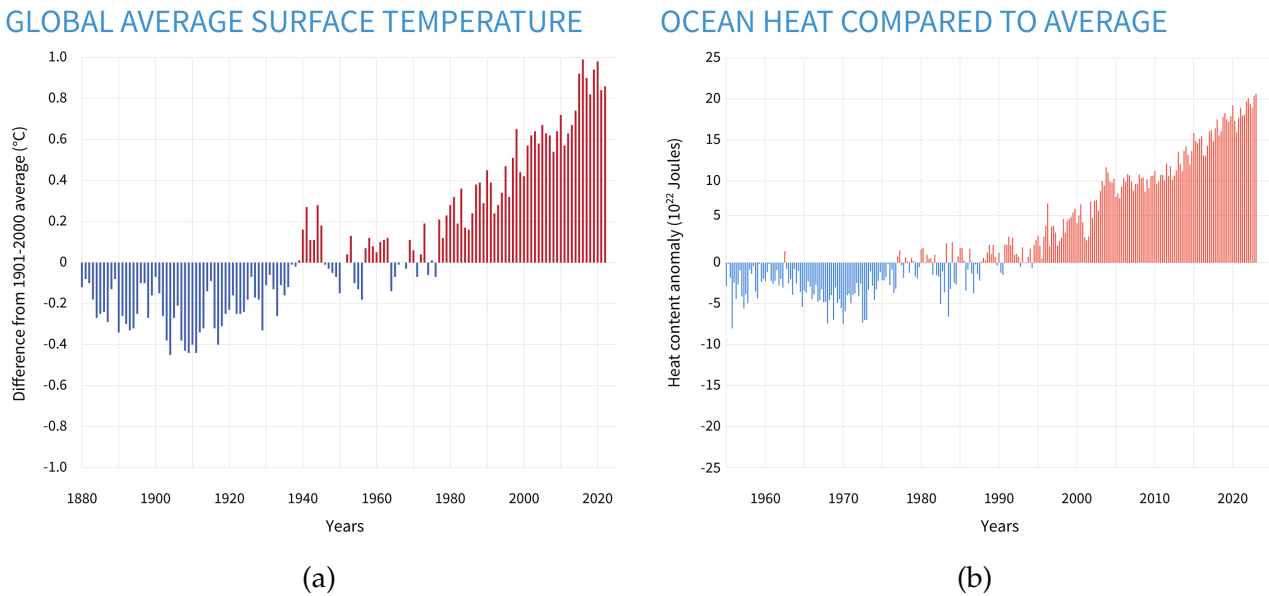


Figure 4.3: The anomalies for (a) Sea Surface Temperature (1880-2022) from 1901-2000 average in °C and (b) 0-700m Ocean Heat Content (1955-2023) from 1955-2006 average. Downloaded from NOAA Climate.gov.

4.2 Case Study Analysis

The path of Hurricane Wilma with the timeseries' of accompanying variables reported in the HURDAT2 dataset is presented in Figure 4.4, along with the calculation for 24 hour DR. The position of Hurricane Wilma at each interval (Figure 4.4a) is plotted using the color corresponding to minimum Central Sea Level Pressure (CSLP), showing the relatively slow movement and large changes in intensity in the early stages of the storms life with respect to that of its subsequent behavior entering the GoM and North Atlantic (not shown). This is further understood inspecting the timeseries' (Figure 4.4b), which show the change in CSLP (left plot) from approximately 980 hPa 18 October to almost 880 hPa on 19 October, and the resulting change in maximum wind speed (middle plot). The corresponding values calculated for DR (Figure 4.4b-right) show the significance of the RI phase during the reported period, without notable phases in the later part of the storms life.

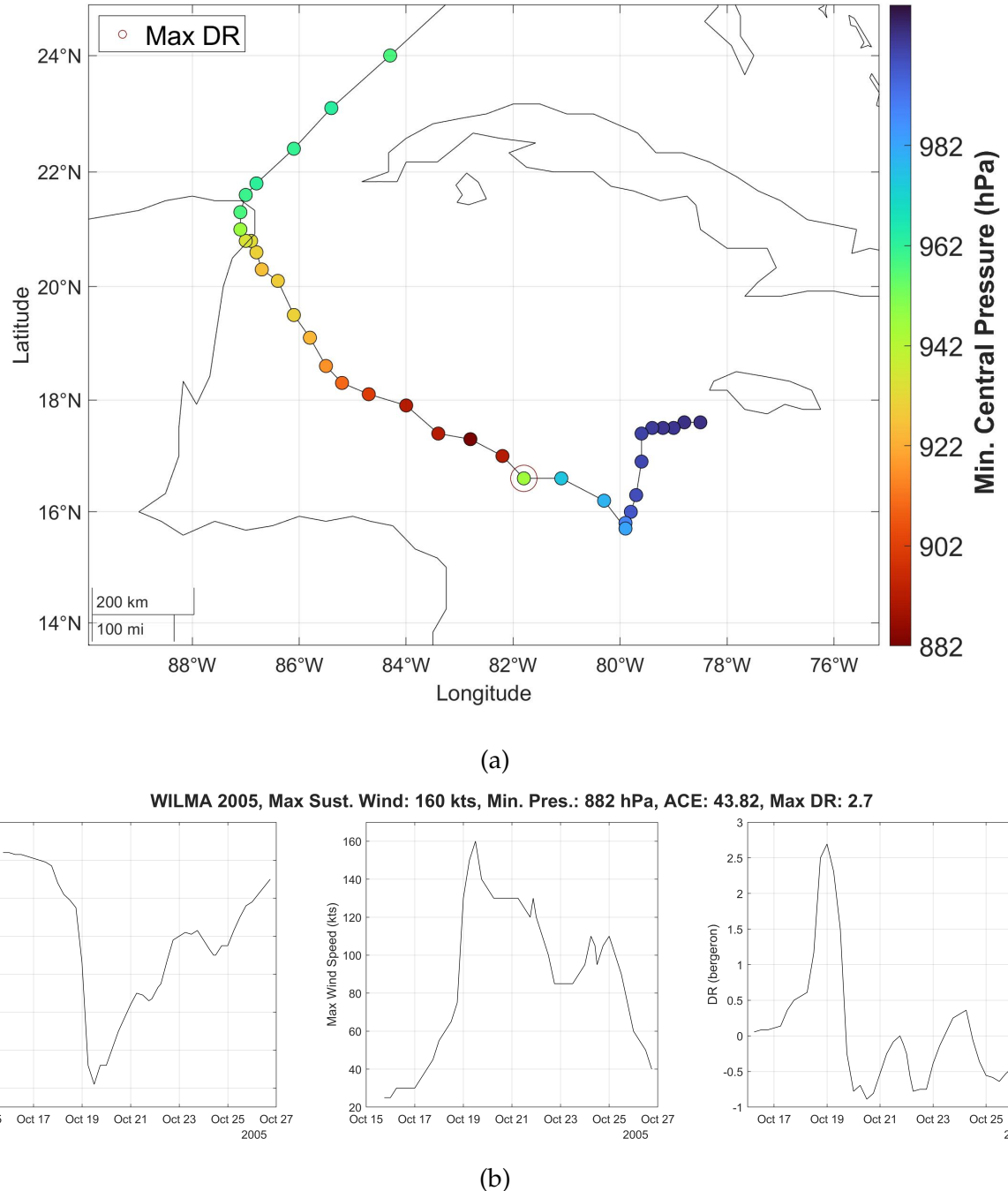


Figure 4.4: Reported observations for Hurricane Wilma showing a) the partial path of the storm with color according to CSLP at each observation and location of maximum DR, and b) the timeseries of CSLP (left), maximum sustained wind speed (middle), and calculated DR (right) derived from the HURDAT2 dataset.

4.2.1 Genesis and Intensification - Synoptic Overview

The state of the atmosphere over the Caribbean Sea prior to the development of the localized disturbance to become Hurricane Wilma consisted of a large monsoon-like trough, as previously noted. The distribution of conditions necessary for TC formation from reanalysis are plotted in Figure 4.5 for 13 October 00UTC, approximately 24 hours prior to the concentrated area of disturbed weather developed. The Mean Sea Level Pressure (MSLP) and 850 hPa temperature (Figure 4.5a) shows a broad distribution of low pressure at the surface from Mexico to the western North Atlantic, with minimum centered west of Jamaica. High values of SST throughout the Caribbean Sea are found (Figure 4.5b), despite the highly active storm season preceding, showing approximately 29-30°C—well exceeding the established SST requirements for cyclogenesis. Vertical wind shear between 500 hPa and 200 hPa over the Caribbean show low values (Figure 4.5c), conducive to vertical development of disturbances. Relative vorticity averaged between 925 hPa to 750 hPa (Figure 4.5d) shows high values of positive vorticity throughout the low, induced by geostrophic like flow around the low pressure trough. The mean lapse rate between 925 hPa and 200 hPa levels (Figure 4.5e) shows values of approximately $-6.5^{\circ}\text{C}/\text{km}$, sufficiently unstable throughout the mid troposphere. Additionally, averaged 925 hPa to 200 hPa relative humidity fields (Figure 4.5f) shows a highly saturated column throughout the trough.

By vertically integrating the specific humidity and multiplying by the mean zonal and meridional velocity, we achieve the vertical Integral of zonal and meridional Water Vapor Flux (IWVF), giving a more comprehensive view of the atmosphere with respect to both humidity and velocity. The IWVF shows a highly saturated column throughout the trough, with the addition of flow vectors showing the geostrophic like flow around the trough. The IWVF field at 18 UTC 13 October in Figure 4.6 shows the trough moved north northeast into the Atlantic and merging with an EC. Additionally, there is an acceleration of the flow

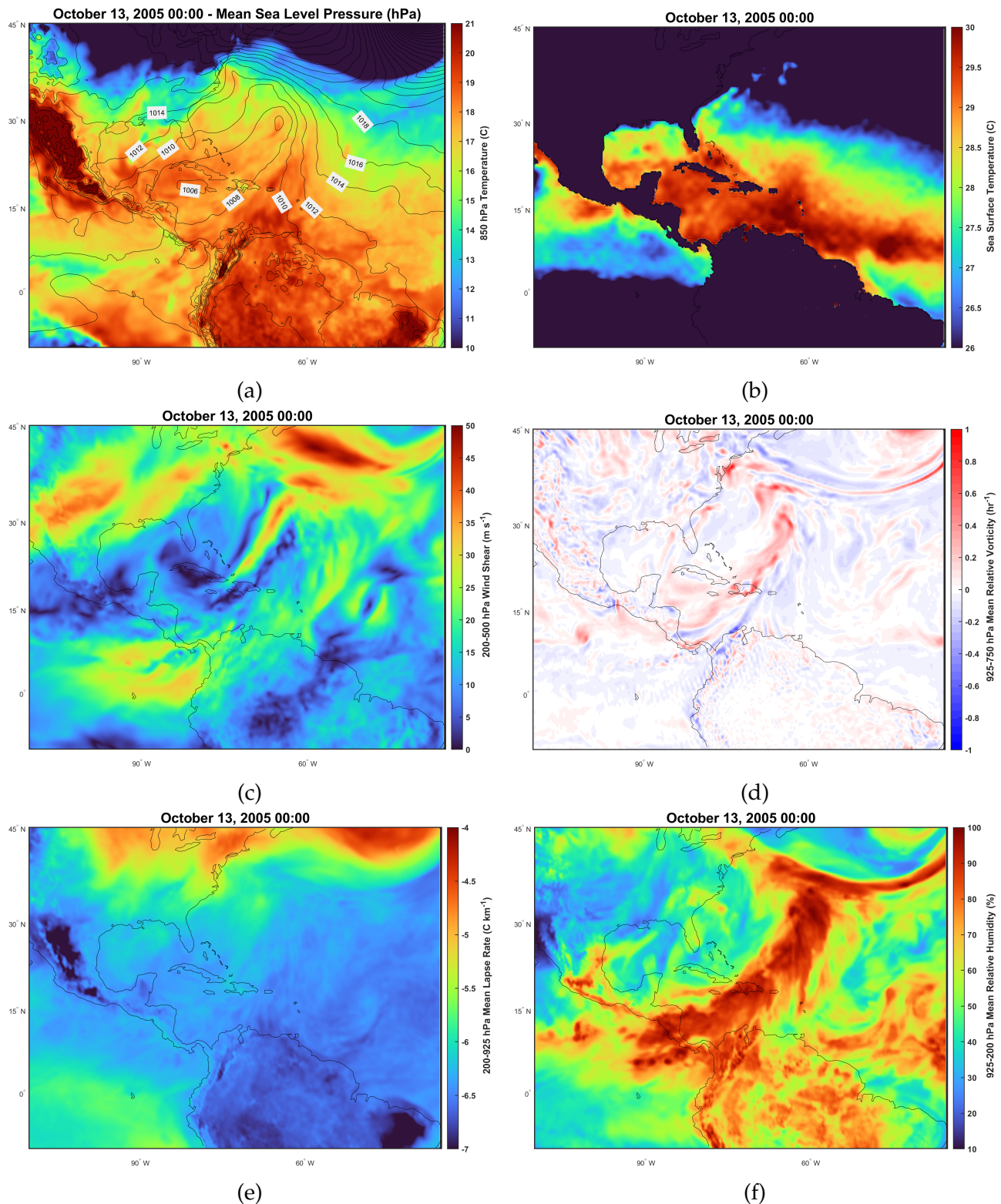


Figure 4.5: Atmospheric parameters conducive to TC formation as reported in Section 2.1, 48 hours before identification of the localized pressure system to later become Hurricane Wilma. Reported values are a) the mean sea level pressure (contours) with 850 hPa temperature (color), b) SST, c) wind shear between the 200 hPa and 500 hPa levels, d) averaged 975 hPa to 750 hPa relative vorticity, e) mean lapse rate between the 975 hPa and 200 hPa levels, and f) averaged 925 hPa to 200 hPa relative humidity, from ERA5 Reanalysis.

in the southern part of the trough, increasing the cyclonic vorticity south of Jamaica due to the southwesterly flow to the north. It is likely this acceleration of flow that induced the formation of the storm to later become Hurricane Wilma.

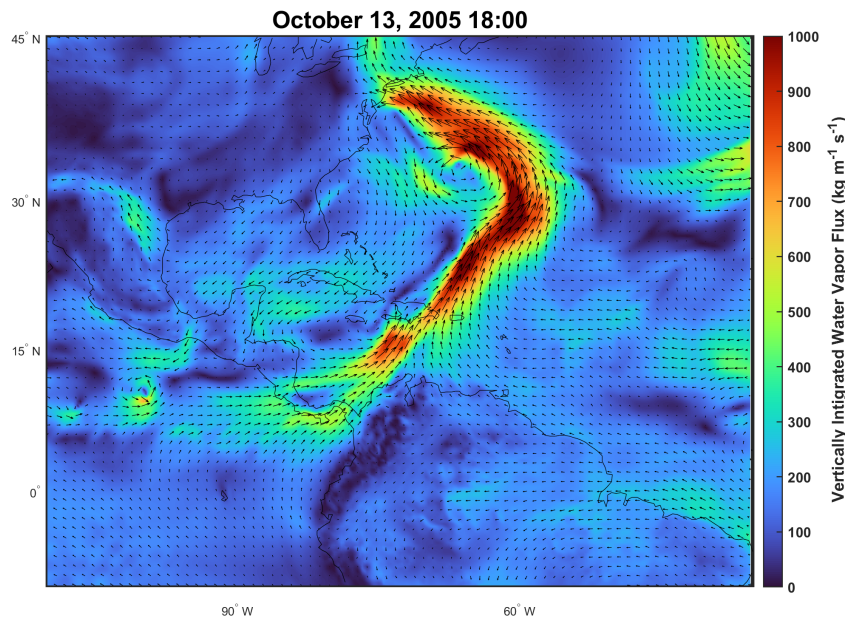


Figure 4.6: Vertically integrated water vapor flux on 12 October 18UTC in both magnitude and vector form, from ERA5 Reanalysis.

The MSLP fields and the 850 hPa temperature (Figure 4.7) clearly shows the evolution of the low pressure system and surrounding areas at the surface as well as the development of the warm core. At 15 October 00UTC a localized low pressure system at the surface begins to form accompanied by warm 850 hPa temperatures throughout the northern Caribbean Sea (Figure 4.7a), this surface low would continue to deepen and be classified as a tropical depression (TD) by 18UTC that day when well defined surface vorticity was observed with CSLP of 1004 hPa. By 17 October 00UTC (Figure 4.7b) the storm moved into the Caribbean, off the western coast of Jamaica. The CSLP at that time was observed to be 1001 hPa; however, a warm core at the 850 hPa has become visible indicating the storm was growing, which would pass the threshold to be classified as a tropical storm (TS) at 06UTC that day. On 18 October 12 UTC the now designated TS Wilma turned northward and strengthened

into a hurricane with CSLP of 979 hPa and surface wind speed of 65 knots ($\sim 33 \text{ ms}^{-1}$). Note that the northward change in direction of a TC typically signifies an increase in intensity (Chan and Chan, 2013). At 18 UTC Hurricane Wilma entered the first part of its RI phase with CSLP of 975 hPa and sustained surface wind speed of 75 knots ($\sim 39 \text{ ms}^{-1}$). Pressure fields (Figure 4.7c) show the continued deepening of the surface low embedded in a synoptic environment of otherwise moderately high MSLP and temperature at 850 hPa slightly more broadly distributed across the center but localized with respect to the surrounding Caribbean environment. By 19 October 00UTC, 6 hours later, CSLP had decreased to 946 hPa and sustained surface wind speeds had increased to 130 knots ($\sim 67 \text{ ms}^{-1}$). At this point the 850 hPa temperature had increased to above 21°C around the core (Figure 4.7d), and the moderately high pressure boundary to the northeast influenced the storms northwestward movement. In the following 6 hours the second phase of the RI took place, where CSLP reached 892 hPa and sustained surface wind speeds of 150 knots ($\sim 77 \text{ ms}^{-1}$) at 06UTC. Pressure fields at that time (Figure 4.7e) indicate elongation of the outer perimeter of the low to the north northwest and south southeast possibly as a result of feedback interaction with the land surfaces of the Yucatan Peninsula of Mexico and Cuba (Zhang et al., 2021; Ahern et al., 2021), as well as initial interaction with the higher pressure areas to the north over the Gulf of Mexico (GoM). The 850 hPa temperature indicates a slight decrease in core temperature as well as a more constricted distribution, which is likely a limitation of the resolution of the reanalysis dataset and the contracted diameter of Wilma's eye at this time of approximately 4 km. Hurricane Wilma reached its observed maximum intensity 6 hours later, at 19 October 12UTC, with CSLP of 882 hPa and sustained surface wind speed of 160 knots ($\sim 82 \text{ ms}^{-1}$).

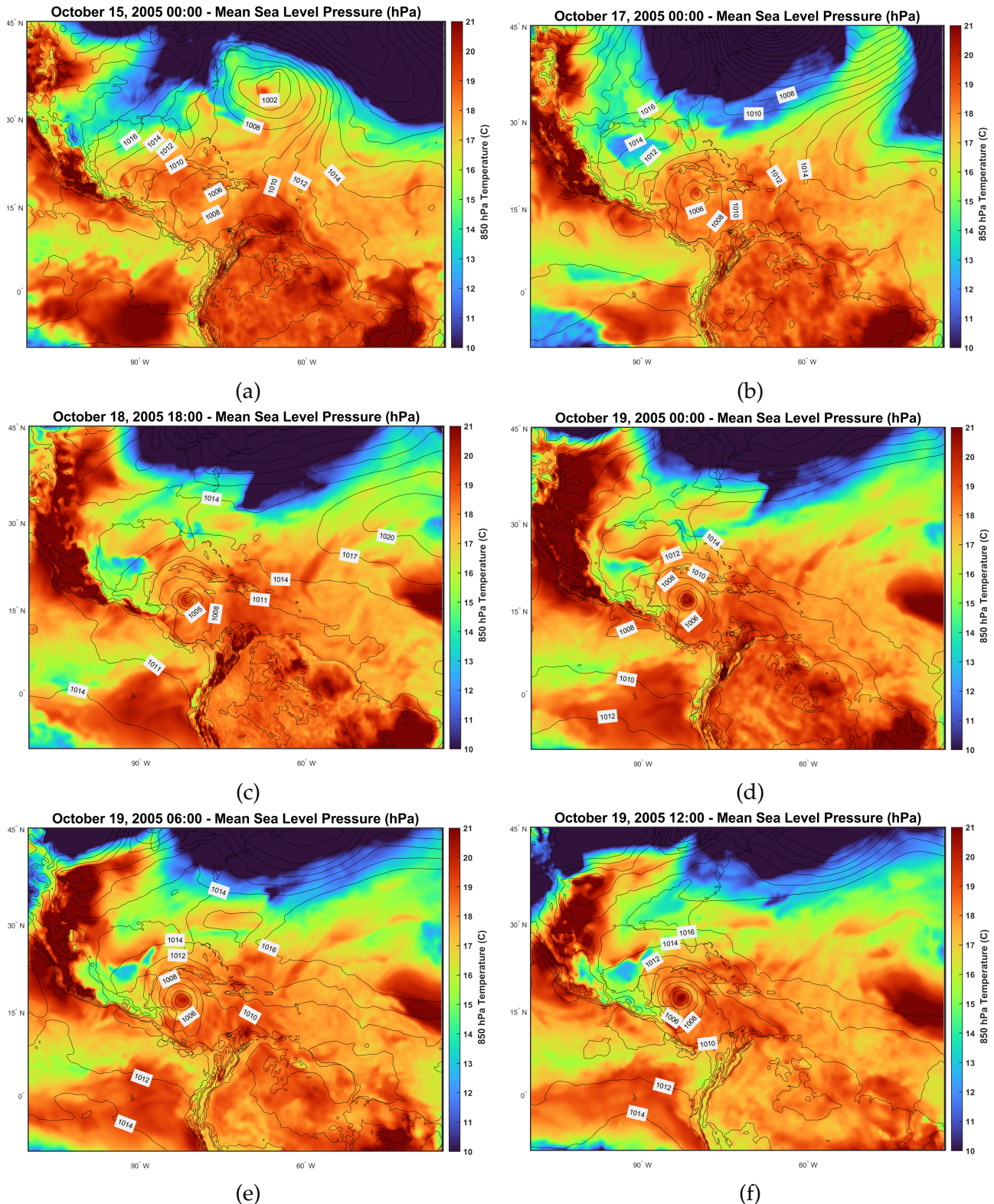


Figure 4.7: Mean Sea Level Pressure (contours) with 850 hPa temperature (color) at a) 15 October 00UTC, b) 17 October 00UTC, c) 18 October 18UTC, d) 19 October 00UTC, e) 19 October 06UTC and f) 19 October 12UTC from ERA5 Reanalysis.

4.2.2 Ocean Analysis

The SSTA fields from ERA5 Reanalysis at four times during Hurricane Wilma's lifetime are presented in Figure 4.8. The SSTA from 15 October 18UTC (Figure 4.8a), the time of TD classification, show that SSTs were anomalously high throughout the Caribbean, most of the GoM, and the majority of the western North Atlantic in comparison to a 1985-2005 baseline. The SSTA at 24 October 00UTC (Figure 4.8b) shows the position of Wilma accelerating toward south Florida, with a "cold wake" shown as a significant difference in the SSTA field trailing.

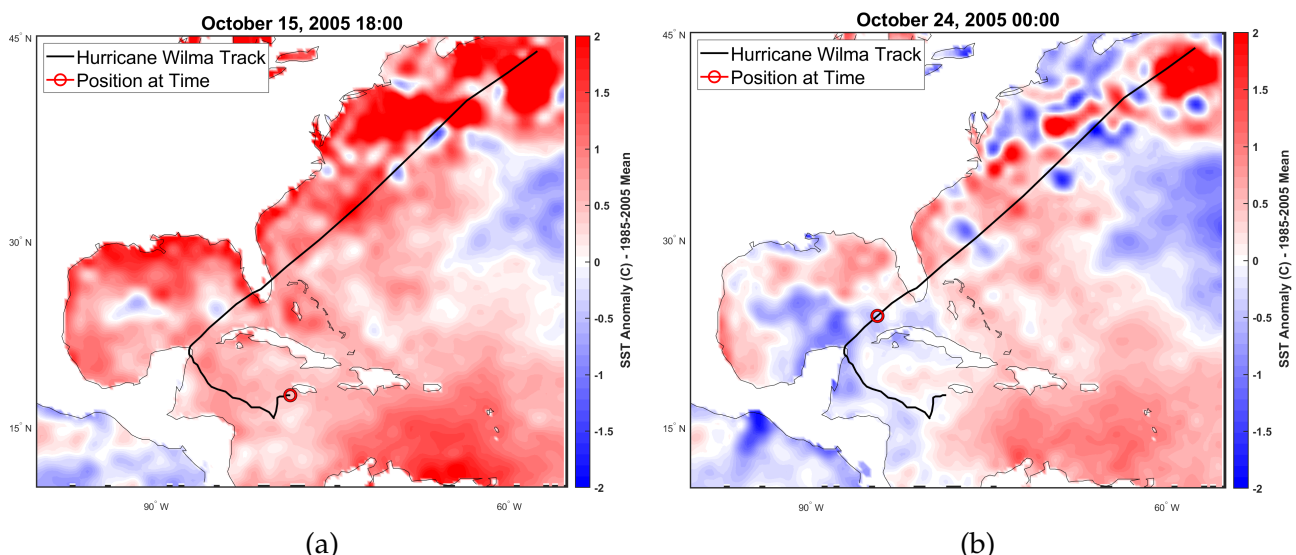


Figure 4.8: Sea Surface Temperature Anomaly in $^{\circ}\text{C}$ for (a) 15 October 18UTC and (b) 24 October 00UTC from 1985-2005 reference mean, calculated from ERA5 reanalysis. Hurricane Wilma track and position at respective times sourced from hurdat dataset.

In addition to the SSTA distribution, the OMLD and OHC are also considered. As shown in Chapter 2, the distribution of OMLD and OHC in the path of an intensifying TC can act as a predictor for intensification potential when paired with a conducive atmosphere. The distribution of OMLD on 18 October (Figure 4.9a), the day where Hurricane Wilma's RI begins, shows a very shallow mixed layer depth south of Jamaica where Wilma was approximately located that morning. However, Wilma's intensification paired with its northwestern movement at the time into an increasingly deep mixed layer (Figures 4.4a, 4.9a) supports the find-

ings that a deepening mixed layer is conducive to greater intensification of TCs. In addition, the distribution of OHC on 18 October (Figure 4.9c) shows high values of OHC in the regions of Wilma's path, with values reaching approximately 150 kJ cm^{-2} along it. Moreover, the D26 was well below the OMLD, so that the entrainment of water into the OML from below by TC induced mixing does not drive the temperature of the mixed layer below the 26°C threshold. These regions with deep D26, and thus high OHC, are potentially responsible for reducing the negative feedback from SST cooling during the following RI phase.

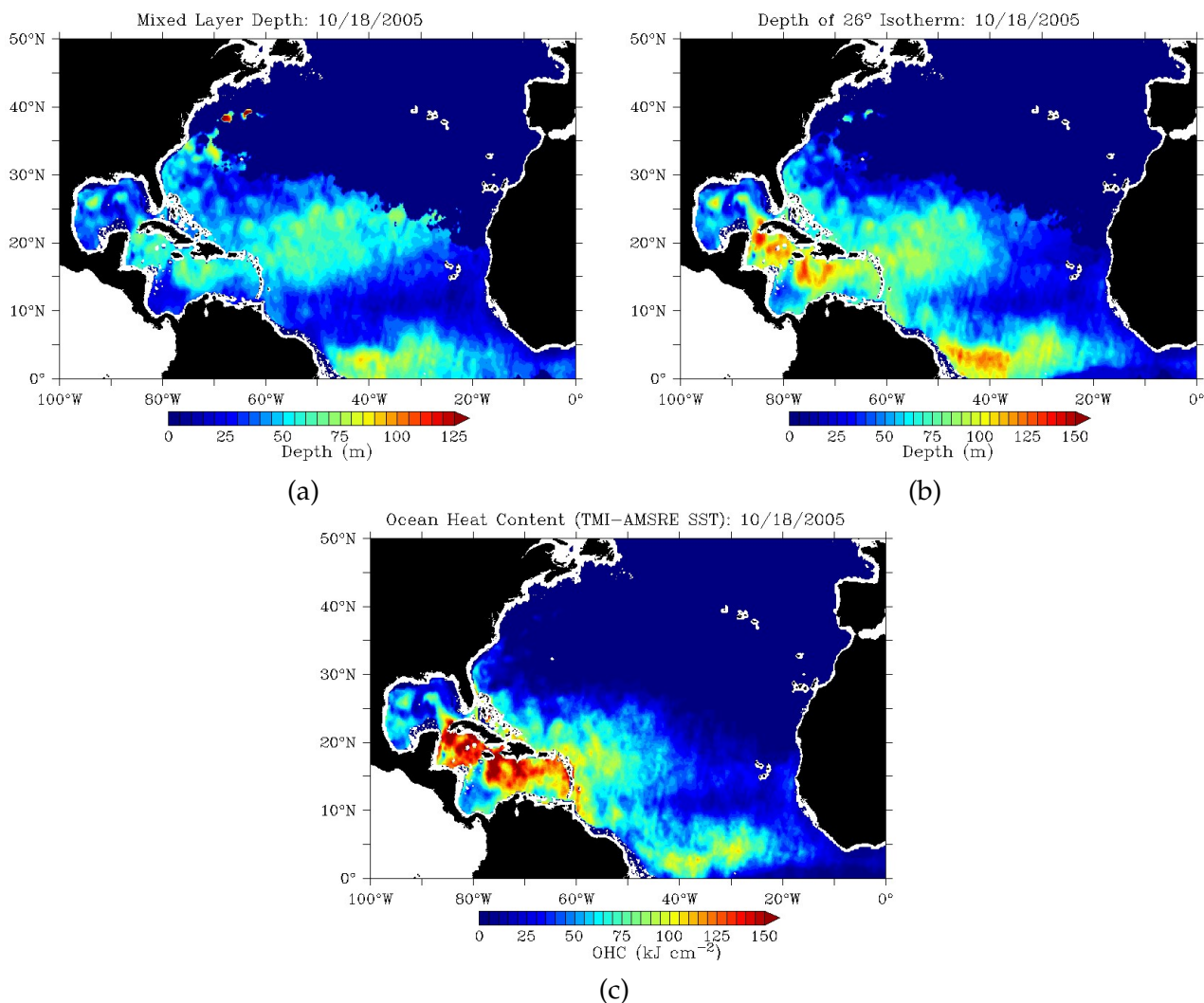


Figure 4.9: The satellite derived (a) Mixed Layer Depth, b) 26°C Isotherm Depth and (c) Ocean Heat Content on 18 October 2005 from NOAA (Donahue, 2015). Downloaded from Miami Rosenstiel School.

5

Simulation Results

The initial numerical simulations of Hurricane Wilma covering the genesis and RI phase from 14 October 00 UTC to 22 October 00 UTC ran until approximately 19 October, at which time a TC had not formed in either case. This shows there is a nontrivial chaotic aspect to the TC formation even when all conditions conducive to formation are met. Therefore a second set of simulations were initialized on 18 October 00UTC, after a substantial TC signal was already present in the initialization data, and run until 22 October 00UTC. These numerical simulations reproduced well the observed RI phase and maximum intensity of Hurricane

Wilma. In the following sections, the simulation initialized with normal SST fields will be referred to as the NORM run, and the simulation initialized with SST fields removing the SSTA will be referred to as the MOD run.

5.1 Initialization Fields

The simulations were initialized with the SST fields as shown in Figure 5.1, where the left plot shows the SST field with observational values, and the right plot shows the SST field after subtracting the 1985-2005 anomaly. As seen in the SSTA field (Figure 4.8), the difference between the two present at this time throughout the Caribbean Sea was approximately +1°C. A noteworthy characteristic of the observed SST field is the warm eddy present in the Caribbean at approximately the position of the observed maximum intensity of Hurricane Wilma.

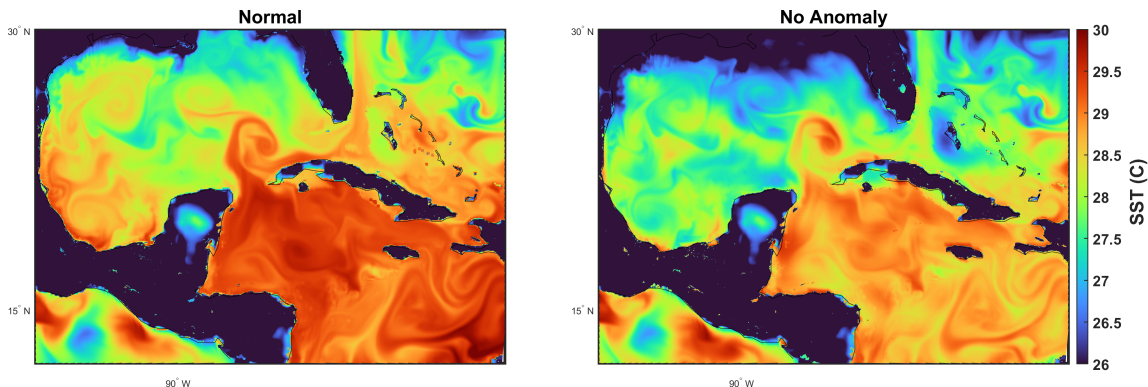


Figure 5.1: Sea surface temperature initialization fields for the two simulations, with the left figure representing the observed SST field and the right figure as the SST field after subtracting the 1985-2005 anomaly.

5.2 Accumulated Cyclone Energy Index

As a preliminary evaluation, the ACE index is considered as a simple metric of the simulations' performance with respect to kinetic energy. Figure 5.2 shows the ACE index calculations for the two simulations along with the calculation from observational values during

the same time period. The calculated for ACE for the NORM and MOD runs were 12.7 and 11.4, respectively. The observational calculations for ACE in the same time period is 24.8. The difference between simulated and observational ACE calculations indicates the model struggled to simulate the observed intensity of Hurricane Wilma, a known problem in numerical models for extreme surface pressure perturbations. Moreover, from the simple ACE metric there is a clear difference between the outcomes of the NORM and MOD runs.

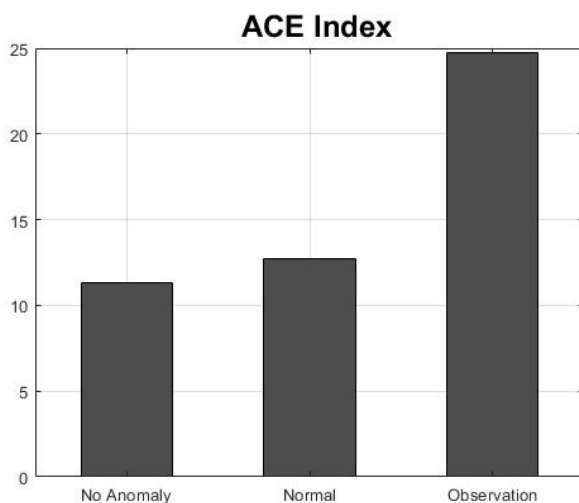


Figure 5.2: Calculations for ACE index for the two simulations and observational values for HURDAT2 during the period 18-22 October 00UTC.

5.3 TC Displacement

The displacement of Wilma is referenced by position of minimum pressure value. The position of Wilma for the two simulations with minimum pressure value indicated by color is shown in Figure 5.3, as well as the observational path during the same period. Both simulations followed closely the observational path during the 40 hour period, after which the paths began to diverge. The MOD run took a more northeasterly route, impacting the western end of Cuba. The NORM run followed closely the observational trajectory but displaced slightly to the northeast, although still impacting the western end of the Yucatan. The velocity of the simulated low was slightly faster than that observed, as is deduced from the final

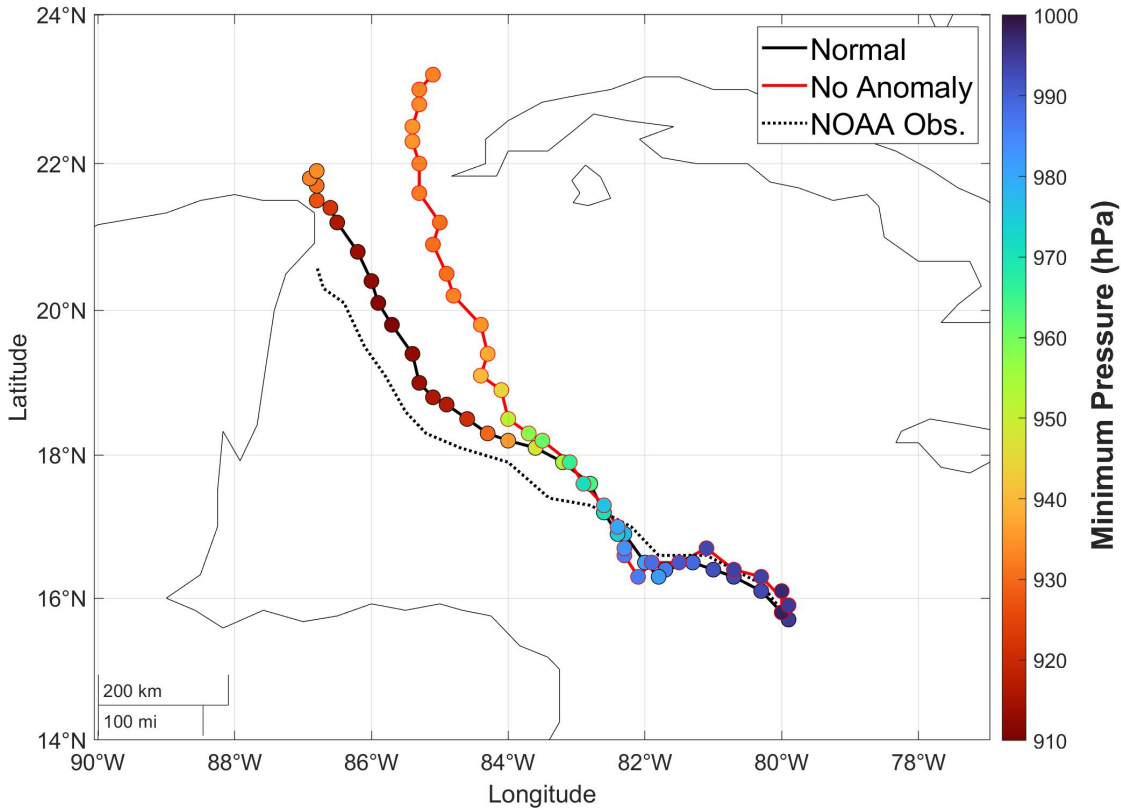


Figure 5.3: Trajectory of minimum pressure (solid lines) with minimum pressure values at each model output time (colored points) for the two simulations. The black solid line indicates the NORM run, and the red solid line indicates the MOD run. The observational trajectory from NOAA during the same time period is also shown as a dotted black line.

position at the end of the simulation period. The faster speed likely impacted the ability of the model produce fully the observed intensity of the TC, with less time spent over regions of high OHC meaning less surface enthalpy flux per time period for TC growth to occur. The shape of the trajectory for both simulations is similar to that of the observed trajectory; however, due to the more northerly component of the translational velocity in the simulations, there was a larger easterly component observed in the displacement from conservation of angular momentum (Coriolis effect). The distance between the two minimum CSLPs was $\sim 230\text{km}$ at the end of the simulation.

5.4 Pressure, Wind and Deepening Rate

The deepening and maximum intensity produced by the model occurred approximately 24 hours later than that of the observed deepening and maximum intensity. The differences in TC produced by the two simulations, and thus the SSTA contribution, are visualized in the timeseries of CSLP, maximum wind speed and DR (Figure 5.4). The timeseries for CSLP (Figure 5.4-left) shows the CSLPs separated early in the simulations; however, both NORM and MOD runs reached their minimum pressure point at 20 October 21UTC of 911 hPa and 931 hPa, respectively. While there is a difference from Wilma's observed minimum pressure of 882 hPa, this outcome is very good considering the challenges associated with a model supporting extreme surface pressure perturbations. The deepening delay provided by the model can be related to the translational velocity, and therefore time length over which enthalpy fluxes are able to supply the TCs growth, and is supported through the characteristic timescale of vortex evolution (Equations 2.5-2.6) with regard to SST and saturation enthalpy of the sea surface. Similarly, the timeseries for maximum wind speed (Figure 5.4-middle) also shows differences between the two simulations. Surprisingly, the difference in maxi-

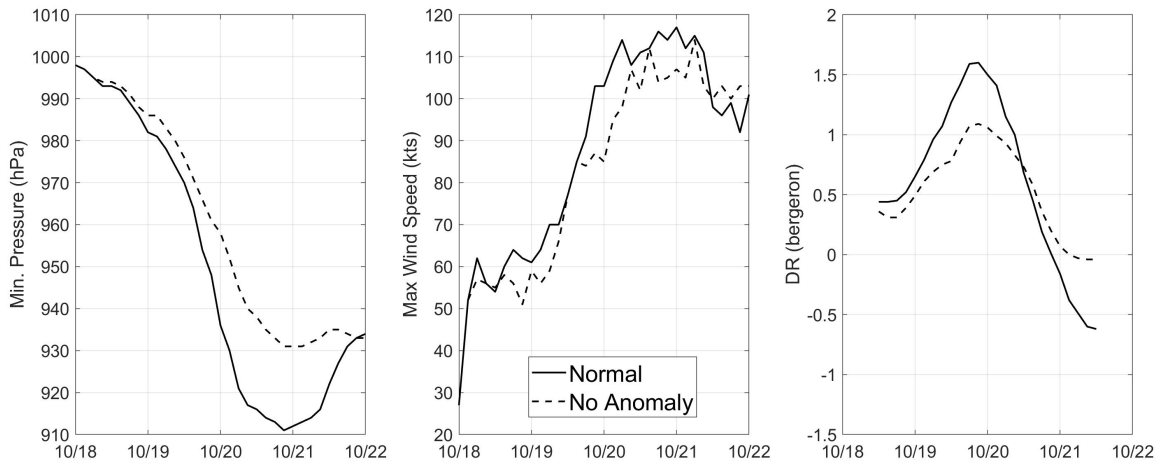


Figure 5.4: Timeseries' of minimum CSLP (left), maximum wind speed (middle) and DR (right) for the two WRF simulations. The solid black line indicates values for the NORM run, and the dashed line indicates values for the MOD run.

mum intensity does not appear proportional to the difference in CSLP. The maximum wind speed reached in the NORM run is 117 knots ($\sim 60 \text{ ms}^{-1}$) at 21 October 00UTC and 114 knots ($\sim 59 \text{ ms}^{-1}$) for the MOD run at 21 October 06UTC. Differences in the two runs of maximum wind speed and time taken to reach that intensity are in agreement with Equations 2.5-2.6. The timeseries for calculated DR are also shown in the right plot of Figure 5.4. The simulated runs reached maximum DR values of 1.6 and 1.1 for the NORM and MOD runs, respectively, at 19 October 21UTC. Additionally, the minimum DR values for the NORM and MOD runs were -0.6 and -0.4, respectively. The DR timeseries shows us 1) that the SSTA present in the NORM run produces higher values of DR and 2) that the onset of the RI phase ($\text{DR} \geq 1$) is delayed approximately 9 hours when the SSTA is removed.

5.5 Heat Flux and Precipitation

The timeseries' for maximum Total Heat Flux at the Surface (THFX) and maximum Accumulated Total Grid Scale Precipitation (RAINNC) are presented in Figure 5.5. This is the maximum value for each respective variable inside a radius of approximately 60 km from the location of minimum pressure at each temporal step. The timeseries for THFX shows the trend for both simulations peaking around the time of maximum intensity, then decreasing. Interestingly, there is a decrease in THFX for the MOD run before maximum intensity is reached, which is also reflected in the maximum wind speed at this time (Figure 5.4-middle). The difference in THFX between the two simulations is largest at 20 October 00UTC during the RI phase and at 21 October 18 UTC just before minimum CSLP in the NORM run is reached, both times having a difference of approximately 1500 W m^{-2} . The differences between THFX in the two simulations results in a much larger difference in total heat transferred when scaled to the size of the TC, which is quantified later on. The differences in values for THFX may be due to the timescale over which the heat flux occurs,

because of the different translational speeds. The timeseries for RAINNC (Figure 5.4-right) shows both simulations have an increasing trend over the period, with RAINNC for the NORM run slightly higher than the MOD run throughout most of the period. A noteworthy point for the MOD run in these timeseries' is at 21 October 06UTC, where there is an increase in RAINNC accompanied by an increase in THFX—a change which is reflected in maximum wind speed but occurs when the CSLP begins to rise. The final values of RAINNC at the end of the simulations (22 October 00UTC) are 850 mm and 774 mm for the NORM and MOD runs, respectively.

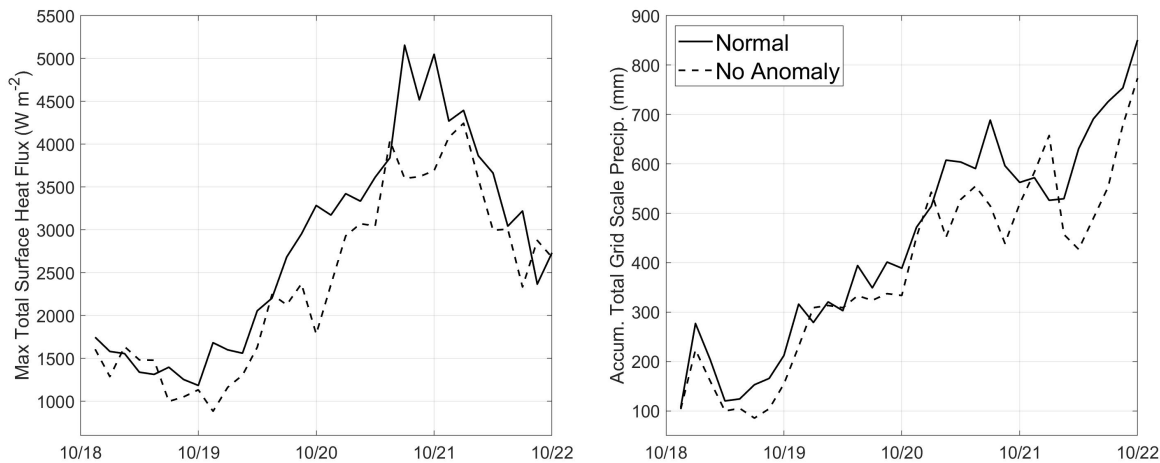


Figure 5.5: Timeseries' of maximum Total Surface Heat Flux (left) and maximum Accumulated Total Grid Scale Precipitation (right) for the two WRF simulations. The solid black line indicates values for the NORM run, and the dashed line indicates values for the MOD run.

The distributions for THFX at the period of maximum intensity, 20 October 21UTC, and RAINNC at the end of the simulation, 22 October 00UTC, are shown in Figure 5.6. Note that the figures for THFX both span 6° of latitude and 6° of longitude. The distribution for THFX (Figure 5.6a) shows a significant difference between the two simulations. Both simulations show approximately the same radius of elevated THFX east and west of the eyewall, although with larger values at the boundaries for the NORM run. However, the NORM run shows THFX above 1000 W m^{-2} extending approximately 1° of latitude further south

of the eyewall. Additionally, maximum values for the NORM run are much larger and distributed more evenly around the eyewall, with maximum values for MOD in front of the TC with respect to the direction of travel. The distribution of RAINNC at 22 October 00UTC

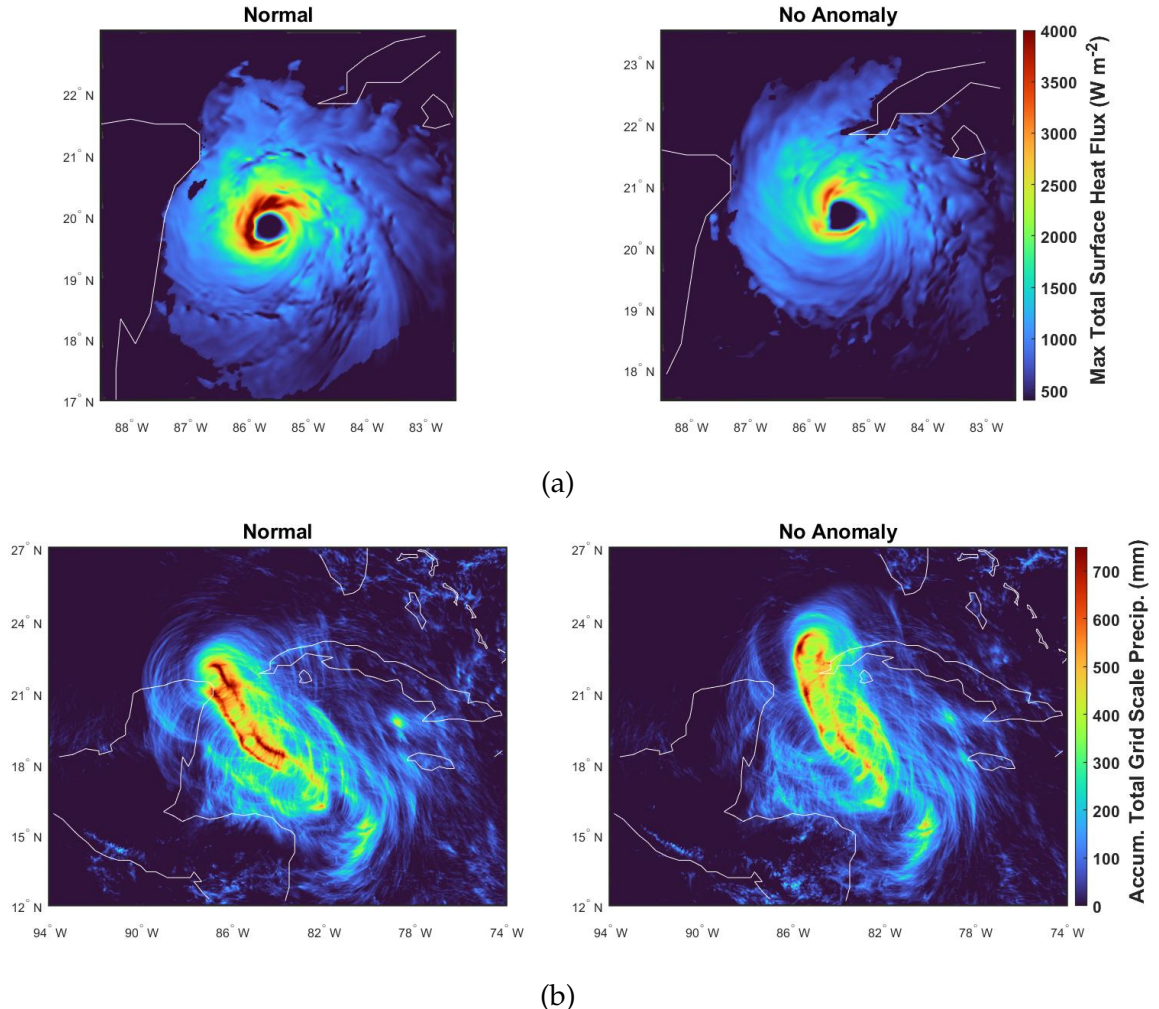


Figure 5.6: WRF simulations results for a) total heat flux at the time of maximum TC intensity (20 October 15 UTC) and b) the accumulate total grid scale precipitation at 22 October 00UTC.

for the two simulations is shown in Figure 5.6b, which clearly shows the path of the TC in each simulation with the highest values of RAINNC lateral to the eyewall in the direction of travel. These lateral trails are also an indication of the TCs intensity, where the trails of large RAINNC values become more distinguished at the locations where the TCs enter their respective RI phases (see Figure 5.3). With the exception of the period where the TCs were turning north early on in the simulations, the values for RAINNC were higher in both sim-

ulations on the southwest side of the TCs, which is consistent with the distribution of THFX being slightly higher to the southwest. This distinction is significant when considering the values for RAINNC at landfall, where the western eyewall in the NORM run impacts the Yucatan with approximately 800 mm of accumulated rain around the coast, and the eastern eyewall in the MOD run impacts the western end of Cuba, with approximately 500 mm of accumulated rain around the coast.

5.6 Energy Extracted from the Surface

The radius from center where elevated THFX occurs is approximately 3° latitude ($\tilde{3}30$ km from bottom edge to center of eye), making a total area approximately $350,000 \text{ km}^2$ over which $\text{THFX} \geq 1000 \text{ W m}^{-2}$ occurs at the TCs maximum intensity. Taking the mean of ele-

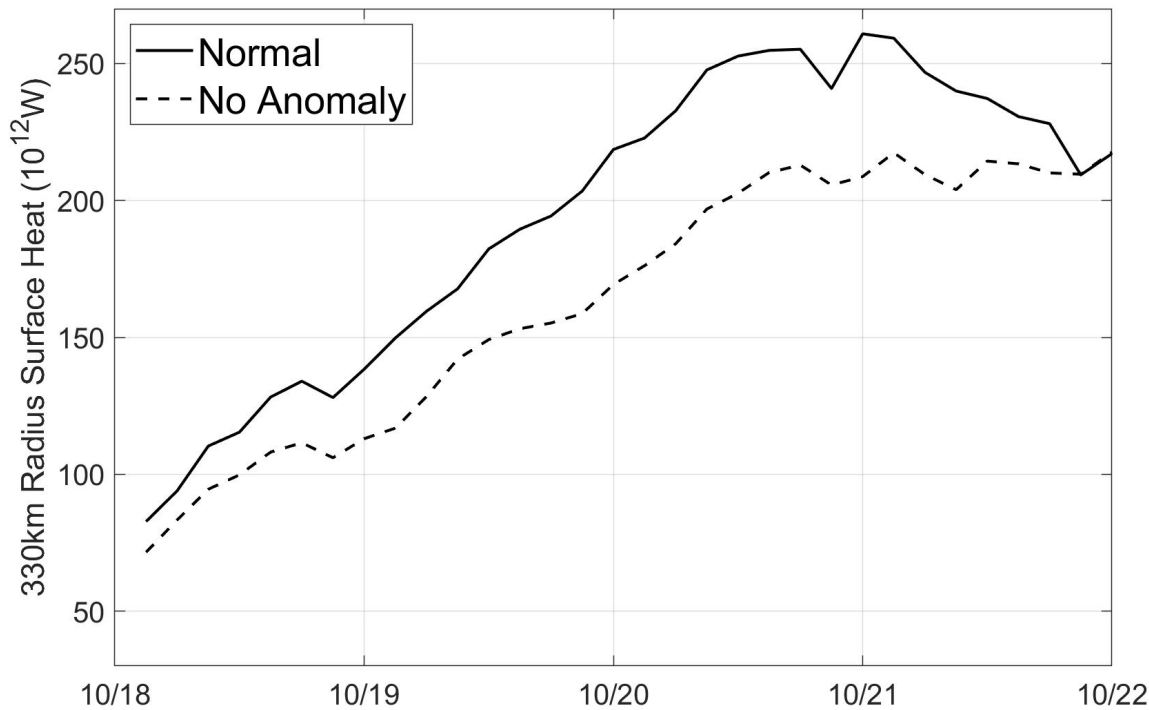


Figure 5.7: Calculated heat transferred from the surface to the atmosphere in a 330 km radius of the minimum CSLP location for the two simulations.

ments inside this radius for each simulation and multiplying by the area, the heat transferred

from the surface to the atmosphere in this region is calculated. The result is approximately 260 TW (10^{12} W) for the NORM run and 209 TW for the MOD run on 21 October 00UTC. The timeseries of this calculation for the simulations are shown in Figure 5.7. The total energy transferred within 330 km radius of the TCs over the entire simulation period is 580 and 489 PJ (10^{15} J) for the NORM and MOD runs, respectively.

5.7 Ocean Mixed Layer Depth

As the model incorporates a dynamic OMLD, the wind driven mixing induced by the TCs can be evaluated with respect to enabling heat extraction. The distribution of OMLD following the TCs in the simulations on 22 October 00UTC are presented in Figure 5.8, showing that the model performed well in incorporating the TC wind driven mixing. Additionally, there is a remarkable difference in the OMLD of the two simulations following the TCs. The NORM run showing OMLD values of approximately 110-120 m from the period of maximum intensity till termination, and the MOD run showing OMLD values of approximately 95-105 m during the same period. The difference in OMLD reported from the two simu-

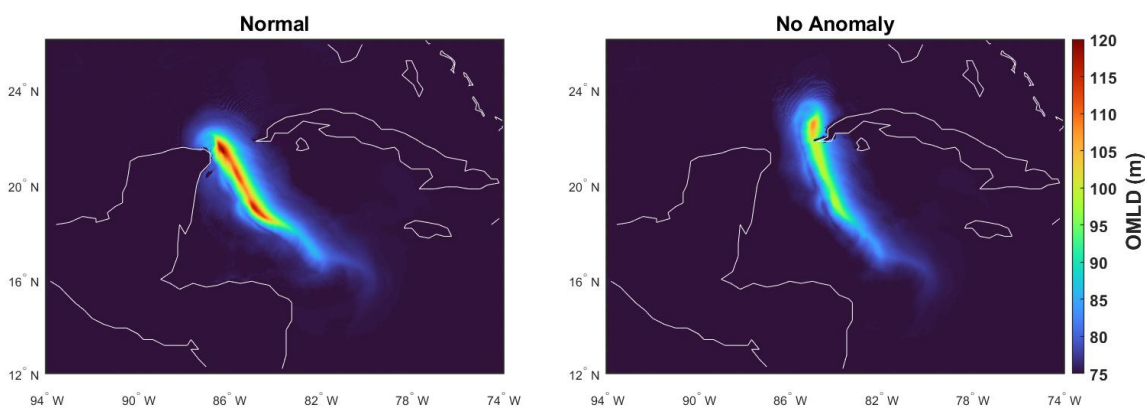


Figure 5.8: WRF simulation results for Ocean Mixed Layer Depth (OMLD) at the end of the simulation period (22 October 00UTC).

lations supports the difference in energy extracted from the sea surface, as reported in the previous section. Moreover, the induced OMLD of approximately 120 m in the NORM run

is very close to reaching the D26 of \sim 125 m, as reported in Figure 4.9b, approaching the limit before cold water entrainment into the mixed layer could begin a negative feedback cycle. However, the observed intensity of Hurricane Wilma being significantly greater than that of the NORM run with respect to maximum wind speed suggests the TC induced mixing likely surpassed this D26. The observed intensity despite of this suggests the high OHC in the region was able to oppose the effects of temperature reduction by cold water entrainment for the given integration time (time spent in a given area).

5.8 Impact of SSTA

From the previous sections, it is clear that the small difference in SST initialization fields as a result of SSTA has an impact on the intensity of a TC. The contribution of the SSTA to the intensity and overall energy extraction has been quantified as a percentage difference between the NORM and MOD results in the timeseries of Figure 5.9. The percentage contribution is displayed as positive for all variables, with the exception of DR, as signifying a contribution to increase in intensity. The difference in CSLP is represented as the deepening produced by the model with respect to the initialization CSLP of 998 hPa. The difference in CSLP produced by the SSTA (Figure 5.9-top left) increased throughout the first half of the simulation and peaked at 20 October 00UTC, just after the period of maximum DR. The SSTA resulted in \sim 55% deeper minimum CSLP following the RI phase, with a smaller difference shown during the minimum CSLPs at \sim 30%. The mean difference in CSLP produced was \sim 27% for the simulation period. The SSTA supported \sim 60% increase in DR (Figure 5.9-center left) at the onset of the the RI phase (19 October 12UTC). The large % difference in DR displayed later on (20-21 October) is a result of the calculated DR for the NORM run approaching and passing through the 0 axis while the DR in the MOD run approaches 0. Additionally, the difference in calculated DR after 21 October 12UTC signifies a much faster dissipation in the

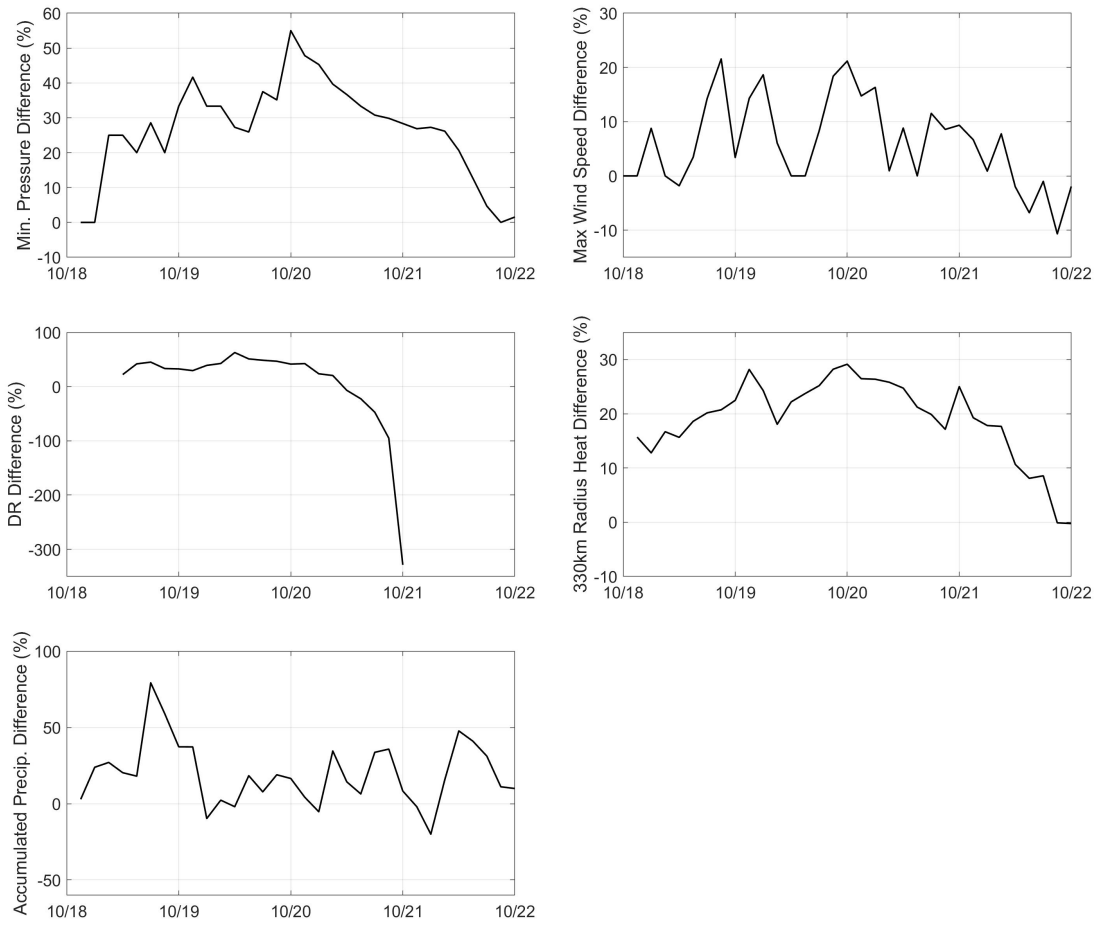


Figure 5.9: The contribution of the SSTA to the intensity and overall energy extraction represented as a percentage difference between the NORM and MOD simulation results.

NORM run following the maximum intensity, as a result of the eyewall in this run making landfall. The mean difference in DR until 20 October 12UTC, during the deepening period, was $\sim 36\%$. The difference in maximum wind speed between the models (Figure 5.9-top right) was greatest early on in the simulation and just following the maximum DR at 20 October 00UTC with a $\sim 21\%$ difference shown. The prior difference of $\sim 21\%$ at 18 October 2UTC is a result of the MOD run showing a temporarily reduced maximum wind speed. The difference in wind speed at the time of minimum CSLP was $\sim 9\%$ and the mean difference in maximum wind speed was $\sim 6\%$. The difference in heat extracted between the two simulations for a 330km radius is presented in the central-right plot of Figure 5.9. Once again,

the greatest difference is shown just following time of maximum DR (20 October 00UTC), with the SSTA supporting a \sim 28% increase in surface heat and an increased surface heat of \sim 17% at the time of maximum intensity. The mean difference in surface heat was \sim 19%. Moreover, the SSTA resulted in a \sim 19% increase for the calculated total energy transferred, as shown in Section 5.6. The difference in RAINNC between the two simulations (Figure 5.9-bottom) varied. The SSTA supported a maximum difference of \sim 73% at 20 October 09UTC, at the end of the RI phase, suggesting the difference in precipitation produced in the two simulations was greatest during the RI phase. The SSTA supported a difference in maximum RAINNC at 22 October 00UTC of \sim 10%, with an average difference of \sim 20% over the simulation period.

6

Conclusion

The purpose of this work was to investigate the conditions producing the rapid intensification (RI) phase and maximum intensity of Hurricane Wilma from the 2005 North Atlantic hurricane season, and assess the overall impact of climate induced sea surface temperature anomalies (SSTAs) on its intensification using numerical model simulations that incorporate the ocean mixed layer depth (OMLD). It was hypothesized that the ocean heat content (OHC) and anomalously high sea surface temperatures (SSTs) present in the Caribbean Sea were the triggering factors to the observed RI phase and maximum intensity. The objective

was therefore to perform numerical simulations of Hurricane Wilma isolating and quantifying the SSTAs contribution.

A preliminary analysis investigated the statistics related to seasonal tropical cyclone (TC) energetics through the Accumulate Cyclone Energy (ACE) and the frequency of observed RI phases. The global trend in SSTA and OHC was taken into consideration. The synoptic and ocean conditions present during the genesis and intensification were examined using European Centre for Medium-Range Weather Forecasts (ECMWF) ERA5 Reanalysis and satellite derived measurements from the National Oceanic and Atmospheric Administration (NOAA). Two numerical simulations were performed using the Weather Research and Forecasting (WRF) model utilizing the Advanced Research WRF (ARW) core. The simulations were initialized with the first using SST fields consistent with observations at the time (NORM run), and the second using SSTs fields where the SSTA from the 1985-2005 reference period was removed (MOD run). This SSTA during this reference period amounted to a difference of approximately 1°C throughout the Caribbean Sea where the RI phase and maximum intensity of Hurricane Wilma were observed. Both SST initialization fields were well above the generally agreed upon threshold of $\sim 26^{\circ}\text{C}$ conducive to TC genesis.

The numerical simulations reproduced well the RI and maximum intensity of Hurricane Wilma. The results of the simulations showed the SSTA contributed to all aspects of the intensity of Hurricane Wilma analyzed, as well as the TCs displacement. The distance between the two minimum central sea level pressures (CSLPs) was $\sim 230\text{km}$ at the end of the simulation. Overall, the SSTA is found to have produced an average of $\sim 27\%$ lower minimum CSLP with respect to the CSLP at initialization (998 hPa) over the simulation period. A $\sim 30\%$ difference in minimum CSLP was produced with the NORM run resulting in a minimum CSLP of 911 hPa and the MOD run with a minimum CSLP of 931 hPa. The SSTA also resulted in a mean difference in maximum wind speed of $\sim 6\%$ where the maximum

wind speeds produced were 117 and 114 knots (~ 60 and 59 ms^{-1}) for the NORM and MOD runs, respectively, but with the simulations producing a maximum wind speed of 114 and 107 knots (~ 59 and 55 ms^{-1}) at the time of minimum CSLP. Additionally, the deepening rate (DR) during the RI phase was increased by $\sim 60\%$ from the SSTA, with a maximum DR of 1.6 and 1.1 Bergeron for the NORM and MOD runs, respectively. The SSTA also potentially increased the rate at which the TC lost intensity (increased minimum CSLP) following the minimum CSLP, but is limited by only the NORM run eyewall making landfall. The maximum total surface heat flux (THFX) produced in the simulations were ~ 5.2 and $\sim 4.2 \text{ kW m}^{-2}$ for the NORM and MOD runs, respectfully. The resulting total energy transferred from the surface in a 330 km radius of the minimum CSLP over the simulation period was increased by $\sim 19\%$ from the SSTA, with 580 PJ (10^{15} J) transferred in the NORM run and 489 PJ transferred in the MOD run. Lastly, the SSTA produced a $\sim 10\%$ increase in accumulated grid scale precipitation (RAINNC), with 851 mm for the NORM run and 774 mm for the MOD run.

The findings of this study show the SST has an impact on both intensity and track of the TC produced by the model, in agreement with previous findings. The resulting differences in the reported values produced by the model were surprisingly high considering the relatively small difference in SST. It is also surprising that the maximum wind speed produced in the two simulations differed by only 3 knots despite having 20 hPa difference in minimum CSLP. This difference in minimum CSLP produced by the model from $\sim 1^\circ \text{C}$ difference in SST doubles the $10 \text{ hPa } ^\circ \text{C}^{-1}$ prediction and is $\sim 61\%$ of the $33 \text{ hPa } ^\circ \text{C}^{-1}$ prediction. The discrepancy is somewhat justified, as this study introduced a reduced SST without the adjusted equilibrium of the atmosphere. It is then reasonable to deduce the contribution of the climate induced SSTA on the observed maximum intensity of Hurricane Wilma as closer to the prediction of $10 \text{ hPa } ^\circ \text{C}^{-1}$. The difference in maximum DR calculated in the

two simulations is consistent with the theoretical framework of characteristic timescale of vortex evolution dependence on SST, and is supported in the findings that higher SSTs produce greater heat fluxes, which induce stronger overturning circulation in the low to middle troposphere and subsequently a more rapid spin up. Additionally, the result that the onset of the RI phase begins earlier in the NORM run, ultimately leading to greater RI (higher max DR) and higher maximum intensity (in terms of minimum CSLP) reflects the results of previous studies. Moreover, the difference in RI onset times of the two simulations is ~ 9 hours, very close to the 13 hours found previously. The calculated energy extracted from the surface for the simulations is on the order of 100 J cm^{-2} for the 330km radius, much less than the 12 kJ cm^{-2} found previously. However, this difference is justified as the reported value considers a smaller area where density of heat flux from the simulations would be greater.

The relatively short time frame in which the frequency and intensity of TCs have been fully accounted for makes it difficult to predict how changes in climate will affect the frequency and intensity of TCs in the future. This study allows insight into a relatively recent and unprecedented RI event in the context of climate induced SSTA, showing that these SSTAs induce higher intensity storms through increased surface enthalpy fluxes. The model producing TCs with large differences in minimum CSLP and DR from only 1°C difference in SST signifies that cases of TCs undergoing extreme RI phases will become more common with increasing SSTs. Moreover, the massive amount of energy extracted from the oceans from intense TCs, even when extrapolated to account for the global average number of TCs per year, is still many orders of magnitude less than the yearly increase of OHC, which further increases the potential for the manifestation of these events.

While the numerical simulations utilized in this study have provided valuable insights into the contribution of surface fluxes to RI events in TCs, several limitations must be acknowledged. Firstly, the resolution of the model and the parameterizations of sub-grid

scale variables introduce inherent uncertainties. The scale at which certain atmospheric and oceanic processes are represented may impact the accuracy of the results. Additionally, the lack of adjustment of atmospheric variables for equilibrium with SSTs introduces simplifications that do not fully capture the complexity of real-world conditions. Furthermore, it's essential to note that the study focused on a singular RI case, limiting the generalization of the findings.

A more comprehensive analysis would benefit from considering multiple cases to account for variability in both TC and synoptic environment characteristics. To enhance the robustness of future studies, it is recommended to utilize coupled models that better identify the mechanisms contributing to RI events and explore how these mechanisms can be integrated into forecasting models for improved prediction of these events. Furthermore, a more in-depth investigation into the joint contribution of surface fluxes and convective bursts to RI events would provide a more holistic understanding of the complex processes influencing TC intensification. These proposed advancements would contribute to refining our comprehension of RI phenomena and improving the accuracy of forecasting models.

Bibliography

- K. Ahern, R. E. Hart, and M. A. Bourassa. Asymmetric hurricane boundary layer structure during storm decay. part i: Formation of descending inflow. *Monthly Weather Review*, 149(11):3851–3874, 2021.
- G. D. Bell, M. S. Halpert, R. C. Schnell, R. W. Higgins, J. Lawrimore, V. E. Kousky, R. Tinker, W. Thiaw, M. Chelliah, and A. Artusa. Climate assessment for 1999. *Bulletin of the American Meteorological Society*, 81(6):S1–S50, 2000.
- T. Bergeron. Review of modern meteorology—12. the problem of tropical hurricanes. *Quarterly Journal of the Royal Meteorological Society*, 80(344):131–164, 1954.
- M. Bister and K. A. Emanuel. Dissipative heating and hurricane intensity. *Meteorology and Atmospheric Physics*, 65:233–240, 1998.
- C. E. Carniel, R. Ferretti, A. Ricchi, G. Curci, M. M. Miglietta, M. Reale, P. Serafini, E. D. Wellmeyer, and D. Zardi. Explosive cyclones in the mediterranean sea exploiting era5 dataset: detection, classification, statistical and synoptic analysis of their occurrence. Technical report, Copernicus Meetings, 2023.
- K. T. Chan and J. C. Chan. Angular momentum transports and synoptic flow patterns associated with tropical cyclone size change. *Monthly weather review*, 141(11):3985–4007, 2013.
- H. Chen and D.-L. Zhang. On the rapid intensification of hurricane wilma (2005). part ii: Convective bursts and the upper-level warm core. *Journal of the Atmospheric Sciences*, 70(1):146–162, 2013.
- H. Chen, D.-L. Zhang, J. Carton, and R. Atlas. On the rapid intensification of hurricane wilma (2005). part i: Model prediction and structural changes. *Weather and Forecasting*, 26(6):885–901, 2011.
- X. Chen, M. Xue, and J. Fang. Rapid intensification of typhoon mujigae (2015) under different sea surface temperatures: Structural changes leading to rapid intensification. *Journal of the Atmospheric Sciences*, 75(12):4313–4335, 2018.
- N. Ćrnivec, R. K. Smith, and G. Kilroy. Dependence of tropical cyclone intensification rate on sea-surface temperature. *Quarterly Journal of the Royal Meteorological Society*, 142(697):1618–1627, 2016.
- R. A. Dare and J. L. McBride. Sea surface temperature response to tropical cyclones. *Monthly Weather Review*, 139(12):3798–3808, 2011.
- M. DeMaria and J. Kaplan. Sea surface temperature and the maximum intensity of atlantic tropical cyclones. *Journal of climate*, 7(9):1324–1334, 1994.

- D. Donahue. Satellite ocean heat content suite, 2015.
- K. Emanuel. Tropical cyclones. *Annual review of earth and planetary sciences*, 31(1):75–104, 2003.
- K. A. Emanuel. An air-sea interaction theory for tropical cyclones. part i: Steady-state maintenance. *Journal of Atmospheric Sciences*, 43(6):585–605, 1986.
- K. A. Emanuel. The maximum intensity of hurricanes. *J. Atmos. Sci*, 45(7):1143–1155, 1988.
- K. A. Emanuel. The finite-amplitude nature of tropical cyclogenesis. *Journal of the Atmospheric Sciences*, 46(22):3431–3456, 1989.
- K. A. Emanuel. Sensitivity of tropical cyclones to surface exchange coefficients and a revised steady-state model incorporating eye dynamics. *Journal of Atmospheric Sciences*, 52(22):3969–3976, 1995.
- T. Glotfelty, K. Alapaty, J. He, P. Hawbecker, X. Song, and G. Zhang. The weather research and forecasting model with aerosol–cloud interactions (wrf-aci): development, evaluation, and initial application. *Monthly weather review*, 147(5):1491–1511, 2019.
- W. M. Gray. Global view of the origin of tropical disturbances and storms. *Monthly Weather Review*, 96(10):669–700, 1968.
- W. M. Gray. Hurricanes: their formation, structure and likely role in the tropical circulation. meteorology over the tropical oceans. *Roy. Meteor. Soc.*, pages 155–218, 1979.
- W. M. Gray. Forecast of atlantic seasonal hurricane activity for 1988, 1988.
- J. R. Gyakum, J. R. Anderson, R. H. Grumm, and E. L. Gruner. North pacific cold-season surface cyclone activity: 1975–1983. *Monthly weather review*, 117(6):1141–1155, 1989.
- H. Hersbach, B. Bell, P. Berrisford, G. Biavati, A. Horányi, J. Muñoz Sabater, J. Nicolas, C. Peubey, R. Radu, I. Rozum, D. Schepers, A. Simmons, C. Soci, D. Dee, and J.-N. Thépaut. Era5 hourly data on pressure levels from 1940 to present. *Copernicus climate change service (c3s) climate data store (cds)*, 10(10.24381), 2023a.
- H. Hersbach, B. Bell, P. Berrisford, G. Biavati, A. Horányi, J. Muñoz Sabater, J. Nicolas, C. Peubey, R. Radu, I. Rozum, D. Schepers, A. Simmons, C. Soci, D. Dee, and J.-N. Thépaut. Era5 hourly data on single levels from 1940 to present. *Copernicus climate change service (c3s) climate data store (cds)*, 10(10.24381), 2023b.
- G. J. Holland. The maximum potential intensity of tropical cyclones. *Journal of the atmospheric sciences*, 54(21):2519–2541, 1997.
- G. J. Holland and M. Lander. The meandering nature of tropical cyclone tracks. *Journal of Atmospheric Sciences*, 50(9):1254–1266, 1993.
- Z. I. Janjić. The step-mountain eta coordinate model: Further developments of the convection, viscous sublayer, and turbulence closure schemes. *Monthly weather review*, 122(5):927–945, 1994.
- F. Judt, R. Rios-Berrios, and G. H. Bryan. Marathon versus sprint: Two modes of tropical cyclone rapid intensification in a global convection-permitting simulation. *Monthly Weather Review*, 151(10):2683–2699, 2023.

- J. Kaplan and M. DeMaria. Large-scale characteristics of rapidly intensifying tropical cyclones in the north atlantic basin. *Weather and forecasting*, 18(6):1093–1108, 2003.
- A. B. Kara, P. A. Rochford, and H. E. Hurlburt. An optimal definition for ocean mixed layer depth. *Journal of Geophysical Research: Oceans*, 105(C7):16803–16821, 2000.
- E. Kleinschmidt. Grundlagen einer theorie der tropischen zyklonen. *Archiv für Meteorologie, Geophysik und Bioklimatologie, Serie A*, 4:53–72, 1951.
- J. A. Knaff, M. DeMaria, C. R. Sampson, J. E. Peak, J. Cummings, and W. H. Schubert. Upper oceanic energy response to tropical cyclone passage. *Journal of climate*, 26(8):2631–2650, 2013.
- C. W. Landsea and J. L. Franklin. Atlantic hurricane database uncertainty and presentation of a new database format. *Mon. Wea. Rev.*, 141:3576–3592, 2013.
- D. F. Leipper. Observed ocean conditions and hurricane hilda, 1964. *Journal of the Atmospheric Sciences*, 24(2):182–186, 1967.
- D. F. Leipper and D. Volgenau. Hurricane heat potential of the gulf of mexico. *J. Phys. Oceanogr.*, 2(3):218–224, 1972.
- K.-S. S. Lim and S.-Y. Hong. Development of an effective double-moment cloud micro-physics scheme with prognostic cloud condensation nuclei (ccn) for weather and climate models. *Monthly weather review*, 138(5):1587–1612, 2010.
- I. Lin, C.-C. Wu, K. A. Emanuel, I.-H. Lee, C.-R. Wu, and I.-F. Pun. The interaction of supertyphoon maemi (2003) with a warm ocean eddy. *Monthly Weather Review*, 133(9):2635–2649, 2005.
- J. S. Malkus and H. Riehl. On the dynamics and energy transformations in steady-state hurricanes. *Tellus*, 12(1):1–20, 1960.
- M. Mandal, U. Mohanty, P. Sinha, and M. M. Ali. Impact of sea surface temperature in modulating movement and intensity of tropical cyclones. *Natural Hazards*, 41:413–427, 2007.
- Q. Mao, S. W. Chang, and R. L. Pfeffer. Influence of large-scale initial oceanic mixed layer depth on tropical cyclones. *Monthly Weather Review*, 128(12):4058–4070, 2000.
- F. Mesinger. Forecasting upper tropospheric turbulence within the framework of the mellor-yamada 2.5 closure. *Res. Activ. Atmos. Oceanic Mod.*, 1993.
- W. Miller, H. Chen, and D.-L. Zhang. On the rapid intensification of hurricane wilma (2005). part iii: Effects of latent heat of fusion. *Journal of the Atmospheric Sciences*, 72(10):3829–3849, 2015.
- E. Palmen. On the formation and structure of tropical hurricanes. *Geophysica*, 3(1):26–38, 1948.
- R. Pasch, E. Blake, H. Cobb, and D. Roberts. Tropical cyclone report. hurricane wilma: 15–25 october 2005. noaa/national weather service, national hurricane center, miami, fla, 2006.
- R. T. Pollard, P. B. Rhines, and R. O. Thompson. The deepening of the wind-mixed layer. *Geophysical Fluid Dynamics*, 4(4):381–404, 1973.

- N. Qin, D.-L. Zhang, W. Miller, and C. Q. Kieu. On the rapid intensification of hurricane wilma (2005). part iv: Inner-core dynamics during the steady radius of maximum wind stage. *Quarterly Journal of the Royal Meteorological Society*, 144(717):2508–2523, 2018.
- H. Ramsay. The global climatology of tropical cyclones, 05 2017. URL <https://doi.org/10.1093/acrefore/9780199389407.001.0001/acrefore-9780199389407-e-79>.
- H. Riehl. On the formation of typhoons. *Journal of the Atmospheric Sciences*, 5(6):247–265, 1948.
- H. Riehl. A model of hurricane formation. *Journal of Applied Physics*, 21(9):917–925, 1950.
- H. Riehl. Some relations between wind and thermal structure of steady state hurricanes. *Journal of Atmospheric Sciences*, 20(4):276–287, 1963.
- P. J. Roebber. Statistical analysis and updated climatology of explosive cyclones. *Monthly Weather Review*, 112(8):1577–1589, 1984.
- F. Sanders and J. R. Gyakum. Synoptic-dynamic climatology of the “bomb”. *Monthly Weather Review*, 108(10):1589–1606, 1980.
- L. R. Schade. Tropical cyclone intensity and sea surface temperature. *Journal of the atmospheric sciences*, 57(18):3122–3130, 2000.
- L. R. Schade and K. A. Emanuel. The ocean’s effect on the intensity of tropical cyclones: Results from a simple coupled atmosphere–ocean model. *Journal of the atmospheric sciences*, 56(4):642–651, 1999.
- L. K. Shay, J. K. Brewster, E. Maturi, D. Donahue, P. Meyers, and C. McCaskill. Algorithm theoretical basis document for satellite derived oceanic heat content product version 3.3, 2022.
- W. C. Skamarock, J. B. Klemp, J. Dudhia, D. O. Gill, D. M. Barker, M. G. Duda, X.-Y. Huang, W. Wang, J. G. Powers, et al. A description of the advanced research wrf version 3. NCAR technical note, 475:113, 2008.
- T. Takemi and S. Yamasaki. Sensitivity of the intensity and structure of tropical cyclones to tropospheric stability conditions. *Atmosphere*, 11(4):411, 2020.
- K. J. Tory and R. A. Dare. Sea surface temperature thresholds for tropical cyclone formation. *Journal of Climate*, 28(20):8171–8183, 2015.
- K. J. Tory, R. Dare, N. Davidson, J. McBride, and S. Chand. The importance of low-deformation vorticity in tropical cyclone formation. *Atmospheric Chemistry and Physics*, 13(4):2115–2132, 2013.
- G. A. Vecchi and B. J. Soden. Effect of remote sea surface temperature change on tropical cyclone potential intensity. *Nature*, 450(7172):1066–1070, 2007.
- V. M. Vincente. An analysis of the rapid intensification of hurricane wilma from the 2005 atlantic hurricane season. 2010.
- A. Wada and J. Chan. Relationship between typhoon activity and upper ocean heat content. *Geophysical Research Letters*, 35(17), 2008.

- C.-C. Wu, C.-Y. Lee, and I. Lin. The effect of the ocean eddy on tropical cyclone intensity. *Journal of the Atmospheric Sciences*, 64(10):3562–3578, 2007.
- A. Yoshida and Y. Asuma. Structures and environment of explosively developing extratropical cyclones in the northwestern pacific region. *Monthly Weather Review*, 132(5):1121–1142, 2004.
- F. Zhang, Z. Pu, and C. Wang. Land-surface diurnal effects on the asymmetric structures of a postlandfall tropical storm. *Journal of Geophysical Research: Atmospheres*, 126(1):2020JD033842, 2021.
- S. Zhang, G. Fu, C. Lu, and J. Liu. Characteristics of explosive cyclones over the northern pacific. *Journal of Applied Meteorology and Climatology*, 56(12):3187–3210, 2017.
- Y. Zheng, K. Alapaty, J. A. Herwehe, A. D. Del Genio, and D. Niyogi. Improving high-resolution weather forecasts using the weather research and forecasting (wrf) model with an updated kain–fritsch scheme. *Monthly Weather Review*, 144(3):833–860, 2016.

A

Eyewall Evolution

The visual evolution of the eyewall for the two simulations is presented here. The evolution with respect to the wind speed is presented in Figure A.1, and with respect to total heat flux in Figure A.2. The plots show successive model outputs at 3 hour intervals. The dimensions of the domain for each plot is 2x2 degrees latitude and longitude, centered on the location of minimum pressure.

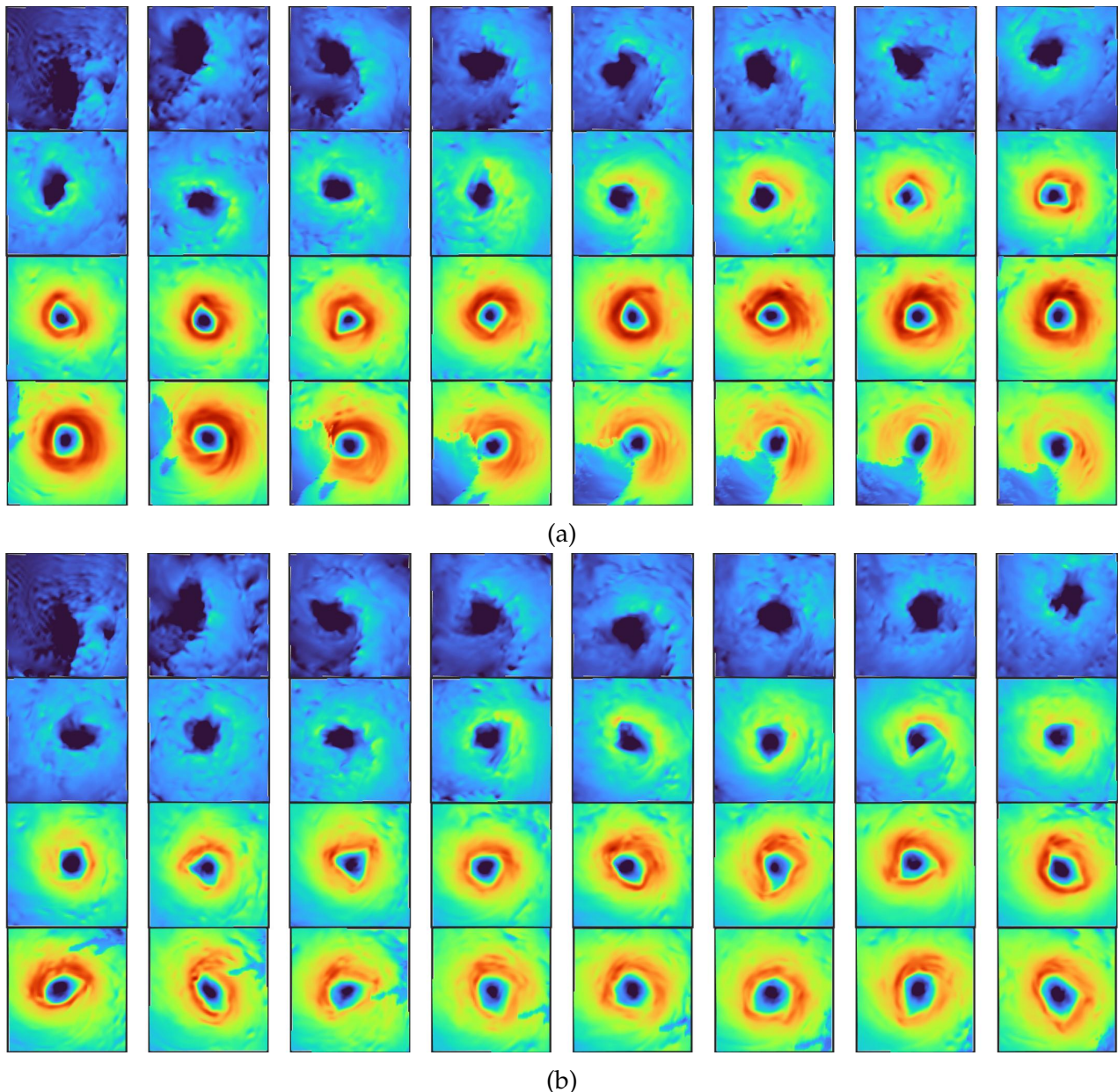


Figure A.1: WRF model outputs showing the evolution of the eyewall at 3 hour intervals with respect to maximum wind speed for a) the simulation using observational SST initialization fields and b) the simulation where the 1985-2005 SSTA has been subtracted.

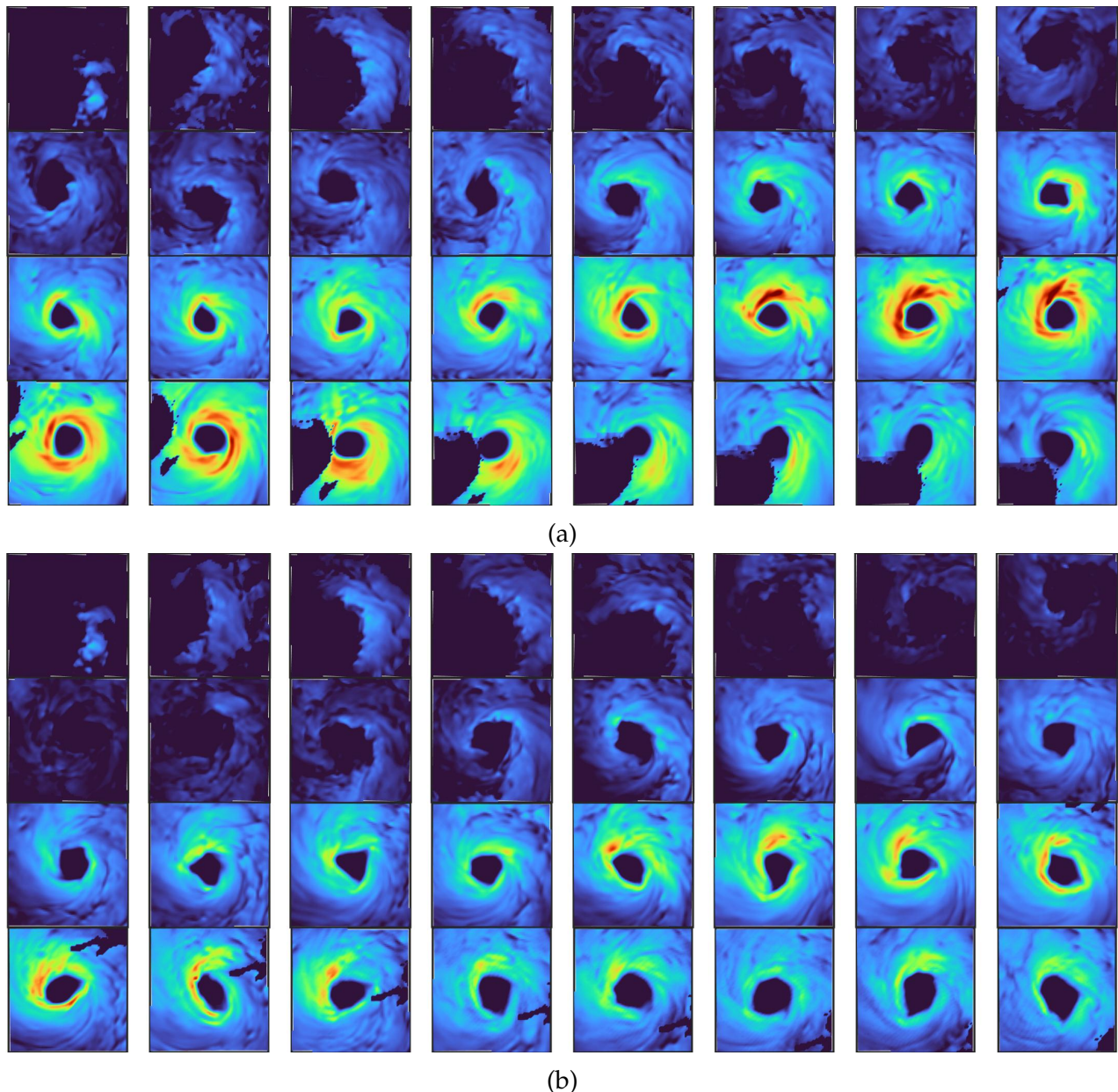


Figure A.2: WRF model outputs showing the evolution of the eyewall at 3 hour intervals with respect to total heat flux for a) the simulation using observational SST initialization fields and b) the simulation where the 1985-2005 SSTA has been subtracted.